Theory of laser-induced associative ionization of ultracold Na

Robert W. Heather and Paul S. Julienne
National Institute of Standards and Technology, Gaithersburg, Maryland 20899
(Received 16 June 1992)

The rate coefficient for the laser-induced associative-ionization reaction of ultracold Na in an optical trap is calculated as a function of the trap laser detuning from the $Na(^2S_{1/2},F=2)\rightarrow Na(^2P_{3/2},F=3)$ resonance. Aided by a knowledge of the excited-state potential-energy curves and of the nature of the free-atom optical-pumping process, we propose the following mechanism, which we call photoassociative ionization (PAI): $2Na(^3\Sigma_u^+)\xrightarrow{\hbar\omega}Na_2^*(0_g^-$ and $1_g)\xrightarrow{\hbar\omega}Na_2^{**}(1_u)\rightarrow Na_2^+ + e^-$. Maxima in the calculated PAI rate coefficient occur at detunings that are simultaneously one-photon resonant with bound levels of the long-range 0_g^- state and two-photon resonant with the lower rotational levels of a vibrational level lying 9 GHz below the dissociation threshold of the autoionizing 1_u state. The calculated PAI spectrum (PAI rate coefficient versus trap-laser detuning) displays a series of broad peaks between -0.5 and -4 GHz detuning and a cutoff at -5 GHz detuning, as does the experimentally measured spectrum of Lett *et al.* [Phys. Rev. Lett. **67**, 2139 (1991)]. The broad widths of the peaks in the PAI spectrum is due in part to the orientation averaging of the collision vector with respect to the electric-field vector and to the optical pumping of the $Na_2\rightarrow Na_2^*$ rovibronic transition. The calculated PAI rate coefficient at -0.6 GHz detuning is a factor of 4 higher than the experimental value. Fine-structure-changing transitions play a role in the doubly excited states, because of the 1_u avoided crossing, but not in the intermediate states, because they have gerade symmetry and the only states that have been shown to undergo fine-structure-changing transitions with large probability have ungerade symmetry. Several predictions based on the proposed model and suggestions for future experiments are discussed.

PACS number(s): 34.50.Fa, 34.50.Rk, 32.80.Pj

I. INTRODUCTION

Currently, there is much interest in using laser light forces to cool and trap neutral atoms [1]. These studies are motivated by a desire to improve time and frequency standards [2] and to study the collision dynamics of ultracold ($T<1$ mK) atoms [3–13]. Collisional loss processes limit the length of time an individual atom spends in the trap, and as a result, limit the density of trapped atoms. Also, collisions may shift and broaden optical transitions of importance in time and frequency standards [14]. Several important features of ultracold collisions include a small velocity spread and long collisional times, both of which should improve the ability to perform high-resolution studies of free-bound transitions, e.g., photoassociation [15]. Indeed, the laser-induced associative-ionization (AI) reaction of Na, $2Na+2\hbar\omega\rightarrow Na_2^+ + e^-$, at ultracold temperatures, is both a trap loss process and an example of photoassociation.

Recently, Lett *et al.* [16] measured the rate of ultracold Na AI in a hybrid optical trap [17]. Their trap employed a rapid alternation between a low-intensity, optical-molasses cooling phase, which utilized Doppler and polarization gradient cooling, and a high-intensity, double-focus trapping phase, which utilized the dipole force. In this manner they were able to cool Na atoms to approximately 0.75 mK at a density of 10^{10} to 10^{11} cm^{-3}, and ion count rates of up to 1 kHz were measured. A large difference in the AI rate coefficient between the trapping and cooling phases, which has been explained by Julienne and Heather [18], is inconsistent with the Na AI mechanism at normal temperatures,

$$2Na(3S)+2\hbar\omega\rightarrow 2Na(3P)\rightarrow Na_2^+ + e^- , \quad (1)$$

in which two Na atoms are resonantly excited at large separations and then collide in a doubly excited electronic state, at small separation ejecting an electron to form Na_2^+. At normal temperatures the rate coefficient (but not the rate) is insensitive to the laser frequency and intensity because the role of the laser is to provide reactants, i.e., Na(3*P*) atoms. However, the normal temperature mechanism does not work at ultracold temperatures because the radiative lifetime of Na(3*P*) (16 ns) is much shorter than the collision time. This suggests that the mechanism at ultracold temperature involves sequential excitation at smaller interatomic separations [11,18], and this causes the rate coefficient to be very sensitive to the laser frequency and intensity. We will call the ultracold process photoassociative ionization (PAI) to distinguish it from the high-temperature process.

Shown in Fig. 1 is the experimentally observed [16] trapping phase Na_2^+ signal as a function of the laser detuning to the red of the $Na(3\,^2S_{1/2},F=2)\rightarrow Na(3\,^2P_{3/2},F=3)$ transition. This type of measurement is an example of photoassociation spectroscopy [15], i.e., measuring the rate of molecular formation from fragments as a function of the laser frequency, and we refer to Fig. 1 as a PAI spectrum. The ion signal cuts off at about -0.5 GHz detuning because the dipole force at shorter wavelengths is too weak to trap the atoms. At

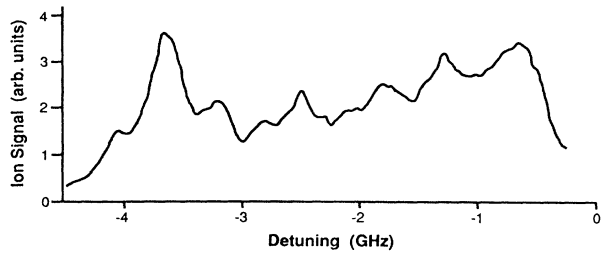

FIG. 1. The experimental Na_2^+ signal vs trap laser detuning (from Ref. [16]).

detunings beyond about -5 GHz, however, the loss of ion signal is not due to the loss of the trap because fluorescence is still observed. Resonance features observed in the ion signal but not in the excited state fluorescence are particularly interesting.

In this paper we investigate the origin of these resonance features by using close-coupling quantal scattering theory to calculate the PAI rate coefficient, as a function of laser detuning, under conditions similar to those in the trapping phase of the hybrid optical trap of Lett *et al.* [16]. Because an exact theoretical description of ultracold Na PAI is an untractable problem at this time, we make simplifications to the exact description, which we attempt to justify on physical grounds. These approximations are made both to reduce the computational effort needed to calculate the PAI spectrum and because of a lack of accurate doubly excited state potentials and their couplings to the molecular ion state.

We begin by restricting our model to a small subset of the ground (labeled Na_2), intermediate (labeled Na_2^*), and doubly excited (labeled Na_2^{**}) molecular electronic states, which correlate at large separation to $Na(3S)+Na(3S)$, $Na(3S)+Na(3P)$, and $Na(3P)+Na(3P)$, respectively. We make an effort to accurately treat the long-range part of the collision, where photon absorption occurs, rather than the short-range part where the doubly excited states autoionize to form Na_2^+: the autoionization step is simulated by coupling the doubly excited states to artificial channels, and the AI rate coefficient is expressed in terms of the transition probabilities from the ground-state entrance channels to the artificial channels. Our choice of the coupling strength between the doubly excited states and the artificial channels is influenced by the theoretical work of Dulieu, Giusti-Suzor, and Masnou-Seeuws [19], as well as the results of high-temperature experiments [20–22].

Further approximations are needed to simplify the theory of ultracold atomic collisions in a laser field. A number of authors have described how excited-state spontaneous emission can play a very important role during the long time scale of an ultracold excited state collision [4–9,11–13]. A proper treatment of such collisions requires solving the Liouville equation of motion for the quantum density matrix [10,13,23] instead of the Schrödinger equation for the wave function. In fact, this must be done to describe PAI in the optical molasses phase of the National Institute of Standards and Technology hybrid trap, where the detuning from the atomic resonance is on the order of a natural linewidth, and the atoms are excited while they are very far apart. Band and Julienne have applied their optical Bloch equation methodology [23] to explain PAI for the small detuning case in optical molasses and cold atomic beams, but this work is planned to be described in a separate publication. The present paper concentrates on describing PAI during the trapping phase, where the trapping laser is detuned by more than 50 natural linewidths and the Rabi frequency is on the order of 100 natural linewidths. In this case, excited-state spontaneous decay can be ignored, and we assume that a Schrödinger equation wave-function description using a conservative Hamiltonian is adequate. This is justified because the atoms are excited when they are close enough together that they ionize before decaying. The vibrational spacing is very large compared to the natural linewidth, and the widths of the bound-state resonances are dominated by stimulated emission and autoionization, not by radiative decay.

Another set of approximations relate to how we describe the full three-dimensional aspects of the problem. First, we investigate the accuracy of predynamically averaging the orientation dependence of the molecule-field interaction in order to remove the dependence of the PAI probability on the projection of the total angular momentum on the space fixed z axis. Summing over projections results in an orientation averaging which broadens the PAI spectrum. Second, we eliminate from the coupling scattering equations rotational branching due to the optical pumping of the $Na_2 \rightarrow Na_2^*$ rovibronic transition, which also broadens the PAI spectrum. We simulate broadening due to orientation averaging and optical pumping by convolving the calculated PAI spectrum with a narrow Lorentzian. Third, we develop a model based on $\Delta J=0$ rather than $\Delta J=0,\pm 1$ selection rules, where J is the total angular momentum quantum number, in order to further reduce the dimensionality of the coupled equations. This approximation is motivated by the fact that the optical transitions occur at large separation where the rotational spacings are small. And fourth, we neglect hyperfine, Coriolis, and other rotational-electronic interactions, but not the spin-orbit interaction. The motivation for making these approximations is to develop a simple but accurate model for investigating the sensitivity of the PAI spectrum to the unknown parameters of the calculation–particularly those associated with the doubly excited states and the autoionization step.

Although the rate coefficient for PAI under strong-field conditions has been calculated by Gallagher using a semiclassical method [11], no resonance structure was found because no molecular bound states were included in his model. In addition, we feel that his model significantly overestimates the role of the intermediate-state fine-structure-changing transitions in diverting flux from the pathway leading to AI.

II. THEORY

The long time and distance scales associated with ultracold collisions complicates the theoretical description.

As was mentioned in the Introduction, if the detuning is sufficiently large, as it is during the trapping phase of the optical trap, then excitation occurs at short enough separation that the duration of the collision while the molecule is in the excited state is much shorter than the natural lifetime and spontaneous emission can be neglected. In this case the role of the long-range optical pumping and spontaneous emission is to prepare steady-state populations of field dressed states [24], and one can describe the collision of atoms in these field dressed states using regular scattering theory with a conservative Hamiltonian. In the close-coupling method, which will now be described, one solves coupled equations to obtained quantities such as the T matrix whose elements are used to calculate the cross section or rare coefficient.

A. Coupled scattering equations

We now derive the coupling scattering equations describing the collision of two Na atoms in a laser field. This involves expanding the total wave function in molecule-plus-field basis functions and scattering wave functions, substituting this wave function into the time-independent Schrödinger equation, left multiplying the Schrödinger equation by the individual basis functions, and integrating over all degrees of freedom other than the internuclear separation R. This results in a coupled second-order differential equation, which is a function of R, that is numerically solved to yield a T matrix, whose elements are labeled by the asymptotic channels. The PAI rate coefficient is calculated by performing the appropriate sum of the square moduli of the T matrix elements for transitions from the entrance channels to the artificial channels which simulate autoionization. This procedure is repeated for each detuning to obtain the PAI spectrum.

The Hamiltonian describing the collision of two atoms in a laser field consists of the following terms:

$$H=H_{\rm el}+V_{\rm s.o.}+T_R+H_{\rm rot}+H_{\rm rad}+V_{\rm rad}\ , \tag{2}$$

where $H_{\rm el}$ is the electronic Hamiltonian, $V_{\rm s.o.}$ is the spin-orbit interaction, T_R is the radial kinetic-energy operator of the nuclei, $H_{\rm rot}$ is the kinetic-energy operator of the rotating molecule, $H_{\rm rad}$ is the Hamiltonian of the laser field, and $V_{\rm rad}$ is the molecule-field interaction. These terms will be described in more detail later.

We begin by expanding the total wave function in terms of molecule-plus-field basis functions of the form

$$\psi_0^{\pm}(J,M,S,|\Lambda|,|\Sigma|,|\Omega|,\alpha,n)=[(2J+1)/8\pi]^{1/2}[\Psi_{\rm el}(S,\Lambda,\Sigma,\Omega,\alpha)D^{J*}_{M,\Omega}\pm\Psi_{\rm el}(S,-\Lambda,-\Sigma,-\Omega,\alpha)D^{J*}_{M,-\Omega}]|n\hbar\omega,\hat{\mathbf{e}}_{+1}\rangle \tag{3}$$

if $\Lambda\neq 0$ or $\Sigma\neq 0$, or

$$\psi_0^0(J,M,S,0,0,0,\alpha,n)=[(2J+1)/4\pi]^{1/2}\psi_{\rm el}(S,0,0,0,\alpha)D^{J*}_{M,0}|n\hbar\omega,\hat{\mathbf{e}}_{+1}\rangle \tag{4}$$

if $\Lambda=0$, $\Sigma=0$, and $\Omega=\Lambda+\Sigma=0$, where $\Psi_{\rm el}(S,\Lambda,\Sigma,\Omega,\alpha)$ are Hund's case (a) Born-Oppenheimer electronic wave functions [25], $D^J_{M,\Omega}$ are the Wigner rotation matrices, and $|n\hbar\omega,\hat{\mathbf{e}}_{+1}\rangle$ are photon number states with n photons of energy $\hbar\omega$ and σ^+ polarization $\hat{\mathbf{e}}_{+1}$. The basis functions are labeled by the total electronic spin S, its projection on the molecular axis Σ (all projections are in units of $\hbar$), the projection of the electronic orbital angular momentum on the molecular axis Λ, the total angular momentum (neglecting nuclear spin) J, and its projection on the space fixed z axis M and molecular axis Ω. α is a collection of labels such as the inversion symmetry (g or u), the reflection symmetry (+ or −, $\Lambda=0$ states only), or any other labels needed to distinguish states that have all the other labels in common. Note that it is important to use basis functions of definite parity—such as those in Eqs. (3) and (4)—when studying collisions between identical particles.

The wave function $\Psi_i(E)$ corresponding to the ith independent solution of the scattering equations at total energy E is expressed as a sum of products of the basis functions in Eqs. (3) and (4) and the to-be-determined scattering wave functions $F_{ji}(R,E)$, i.e.,

$$\Psi_i(E)=\sum_j \psi_0(j)F_{ji}(R,E)/R\ , \tag{5}$$

where i and j are collective indices for different values of J, M, S, Λ, Σ, Ω, α, n, and parity. Spontaneous emission is omitted by including in the wave-function expansion only photon states corresponding to stimulated processes.

Upon substituting $\Psi_i(E)$ into the time-independent Schrödinger equation, left multiplying by $\psi_0(i)$, and integrating over all coordinates other than R one obtains the coupled scattering equations:

$$(E-H_{ii})F_{ii}(R,E)=\sum_j H_{ij}F_{ji}(R,E)\ . \tag{6}$$

How one obtains the PAI spectrum from the solution of Eq. (6) will be discussed in Sec. IV.

B. Molecular electronic states

In order to calculate the $H_{ij}=\langle\psi_o(i)|H|\psi_o(j)\rangle$ matrix elements in Eq. (6) one needs Hund's case (a) electronic wave functions $\Psi_{\rm el}(S,\Lambda,\Sigma,\Omega,\alpha)$, valid when $H_{\rm el}\gg V_{\rm s.o.}$, corresponding to the electronic states that correlate at large separation to Na(3S)+Na(3S), Na(3S)+Na(3P), and Na(3P)+Na(3P). The calculation of molecular electronic wave functions—especially excited-state electronic wave functions—is a difficult task. However, we are aided by the fact that because the trap laser detuning Δ is small ($|\Delta|<5$ GHz), photon absorption occurs at large separation ($R>50a_0$) where there is negligible overlap of the electron charge distributions of each atom. At large separations the electronic wave functions can be expressed as properly symmetrized combinations of Na 3S and 3P or-

bital wave functions and electronic-spin wave functions. The long-range potentials can then be calculated using these wave functions and the multipolar expansion of the Coulomb interaction: states that correlate to Na(3S)+Na(3S) interact by a R^{-6} van der Waals interaction, states that correlate to Na(3S)+Na(3P) interact by a long-range R^{-3} resonant dipole-dipole interaction, and states that correlate to Na(3P)+Na(3P) interact by a R^{-5} quadrupole-quadrupole interaction. A knowledge of the long-range electronic wave functions also allows one to calculate the off diagonal couplings in Eq. (6) due to $H_{\rm rot}$, $V_{\rm s.o.}$, and $V_{\rm rad}$.

1. Ground states

Two ground-state ($3\,^2S$) Na atoms can collide in either a $^1\Sigma_g^+$ or a $^3\Sigma_u^+$ molecular electronic state, where the term symbol Σ denotes that $\Lambda=0$, where Λ is the projection of the electronic orbital angular momentum on the molecular axis, the superscripts 1 and 3 indicate the total electronic spin multiplicity $2S+1$, with spin quantum number $S=s_1+s_2=0$ or 1, the subscripts g and u indicate that the wave function has even (gerade) or odd (ungerade) inversion symmetry, and superscript + indicates that the wave function has even reflection symmetry in a plane containing the nuclei ($\Lambda=0$ states only). The long-range electronic wave functions can be expressed as

$$\Psi_{\rm el}(^1\Sigma_g^+)=(2)^{-1/2}[S^A(1)S^B(2)+S^A(2)S^B(1)]\,^1\chi_{\Sigma=0} \tag{7}$$

for the $^1\Sigma_g^+$ state and

$$\Psi_{\rm el}(^3\Sigma_u^+)=(2)^{-1/2}[S^A(1)S^B(2) -S^A(2)S^B(1)]^3\chi_{\Sigma=0,\pm1} \tag{8}$$

for the $^3\Sigma_u^+$ state, where, for example, $S^A(1)$ denotes a Na 3S orbital wave function centered on atom A, which is a function of the coordinates of (3S) electron 1. The singlet electronic spin wave function is

$$^1\chi_{\Sigma=0}=(2)^{-1/2}(|m_{s_1}=-\tfrac{1}{2},m_{s_2}=\tfrac{1}{2}\rangle -|m_{s_1}=\tfrac{1}{2},m_{s_2}=-\tfrac{1}{2}\rangle) \tag{9}$$

and the triplet electronic spin wave functions are

$$^3\chi_{\Sigma=1}=|m_{s_1}=\tfrac{1}{2},m_{s_2}=\tfrac{1}{2}\rangle\ , \tag{10}$$

$$^3\chi_{\Sigma=0}=(2)^{-1/2}(|m_{s_1}=-\tfrac{1}{2},m_{s_2}=\tfrac{1}{2}\rangle +|m_{s_1}=\tfrac{1}{2},m_{s_2}=-\tfrac{1}{2}\rangle)\ , \tag{11}$$

and

$$^3\chi_{\Sigma=-1}=|m_{s_1}=-\tfrac{1}{2},m_{s_2}=-\tfrac{1}{2}\rangle\ , \tag{12}$$

where m_{s_1} and m_{s_2} are the projections of the spin angular momentum of electrons 1 and 2 on the molecular axis, and $\Sigma=m_{s_1}+m_{s_2}$. The molecular potentials

$$V_{^1\Sigma_g^+}(R)=\langle\Psi_{\rm el}(^1\Sigma_g^+)|H_{\rm el}|\Psi_{\rm el}(^1\Sigma_g^+)\rangle\ ,$$

$$V_{^3\Sigma_u^+}(R)=\langle\Psi_{\rm el}(^3\Sigma_u^+)|H_{\rm el}|\Psi_{\rm el}(^3\Sigma_u^+)\rangle$$

have been calculated at short range by Konowalow, Rosenkranz, and Olson [26], and by Jeung [27], and behave at long range as C_6/R^6.

2. Intermediate states

Eight Hund's case (a) electronic states labeled by the term symbols $^1\Sigma_g^+$, $^3\Sigma_g^+$, $^1\Pi_g$, $^3\Pi_g$, $^1\Sigma_u^+$, $^3\Sigma_u^+$, $^1\Pi_u$, and $^3\Pi_u$ correlate at long range to Na(3S)+Na(3P), where Π denotes states with $\Lambda=\pm1$. The long-range wave functions for these states are of the form [28]

$$\Psi_{\rm el}=\tfrac{1}{2}[S^A(1)P_\Lambda^B(2)+c_1S^A(2)P_\Lambda^B(1)+c_2S^B(1)P_\Lambda^A(2) +c_1c_2S^B(2)P_\Lambda^A(1)]^{2S+1}\chi_\Sigma\ , \tag{13}$$

where, for example, $P_\Lambda^B(1)$ represents a Na 3P orbital wave function on atom B, which is a function of the coordinates of electron 1, with a projection of the orbital angular momentum on the molecular axis $\Lambda=0,\pm1$. In Eq. (13), $\Lambda=0$ for Σ states and ±1 for Π states, $c_1=+1$ for singlets ($S=0$) and -1 for triplets ($S=1$), and $c_2=+1$ for ungerade states and -1 for gerade states. The short-range potentials for these states have also been calculated by Konowalow, Rosenkrantz, and Olson [26] and by Jeung [27], and experimentally determined RKR potentials exist for the $^1\Sigma_u^+$ and $^1\Pi_u$ states [29,30].

The long-range interaction is a resonant dipole-dipole interaction,

$$V_d=e^2[(\mathbf{r}_1\cdot\mathbf{r}_2)-3(\mathbf{r}_1\cdot\hat{\mathbf{z}})(\mathbf{r}_2\cdot\hat{\mathbf{z}})]/R^3\ , \tag{14}$$

where e is the electron charge, $\mathbf{r}_1$ and $\mathbf{r}_2$ are the position vectors of electrons 1 and 2, and $\hat{\mathbf{z}}$ is a unit vector along the molecular axis. The long-range potentials can be determined using Eq. (13) and the following relation [28]:

$$V_\Lambda(R)=\langle S^A(1)P_\Lambda^B(2)|V_d|S^B(2)P_\Lambda^A(1)\rangle =\begin{cases}d^2/R^3 & \text{if } \Lambda=\pm1\\ -2d^2/R^3 & \text{if } \Lambda=0\end{cases} \tag{15}$$

where $d=e\langle S(1)|\mathbf{r}_1|P_0(1)\rangle$ is the transition dipole for the $3S\rightarrow3P$ transition, and the intermediate state potentials are

$$V_{S+P}(R)=c_1c_2V_\Lambda(R)\ . \tag{16}$$

3. Doubly excited states

Twelve Hund's case (a) electronic states labeled by the term symbols $^1\Delta_g$, $^3\Delta_u$, $^1\Pi_g$, $^3\Pi_u$, $^1\Pi_u$, $^3\Pi_g$, $^1\Sigma_u^-$, $^3\Sigma_u^-$, $^1\Sigma_g^+(\sigma\sigma)$, $^3\Sigma_u^+(\sigma\sigma)$, $^1\Sigma_g^+(\pi\pi)$, and $^3\Sigma_u^+(\pi\pi)$ correlate at large separation to Na(3P)+Na(3P), where Δ denotes states with $\Lambda=\pm2$, the superscript $-$ indicates that the wave function has odd symmetry with respect to reflection in a plane containing the nuclei, and $\sigma\sigma$ and $\pi\pi$ are used to differentiate states of σ or π orbital character, but with the same term symbols. The long-range

TABLE I. Hund's case (a) long-range electronic wave functions of the doubly excited state.

Term symbol	Wave functions
$^1\Delta_g$	$\Psi_{el}(\Lambda=2)=^1\Theta_{1,1}/\sqrt{2}$, $\Psi_{el}(\Lambda=-2)=^1\Theta_{-1,-1}/\sqrt{2}$
$^3\Delta_u$	$\Psi_{el}(\Lambda=2)=^3\Theta_{1,1}/\sqrt{2}$, $\Psi_{el}(\Lambda=-2)=^3\Theta_{-1,-1}/\sqrt{2}$
$^1\Pi_g$	$\Psi_{el}(\Lambda=1)=(^1\Theta_{0,1}+^1\Theta_{1,0})/2$, $\Psi_{el}(\Lambda=-1)=(^1\Theta_{0,-1}+^1\Theta_{-1,0})/2$
$^3\Pi_u$	$\Psi_{el}(\Lambda=1)=(^3\Theta_{0,1}+^3\Theta_{1,0})/2$, $\Psi_{el}(\Lambda=-1)=(^3\Theta_{0,-1}+^3\Theta_{-1,0})/2$
$^1\Pi_u$	$\Psi_{el}(\Lambda=1)=(^1\Theta_{0,1}-^1\Theta_{1,0})/2$, $\Psi_{el}(\Lambda=-1)=(^1\Theta_{0,-1}-^1\Theta_{-1,0})/2$
$^3\Pi_g$	$\Psi_{el}(\Lambda=1)=(^3\Theta_{0,1}-^3\Theta_{1,0})/2$, $\Psi_{el}(\Lambda=-1)=(^3\Theta_{0,-1}-^3\Theta_{-1,0})/2$
$^1\Sigma_u^-$	$\Psi_{el}(\Lambda=0)=(^1\Theta_{1,-1}-^1\Theta_{-1,1})/2$
$^3\Sigma_g^-$	$\Psi_{el}(\Lambda=0)=(^3\Theta_{1,-1}-^3\Theta_{-1,1})/2$
$^1\Sigma_g^+(\sigma\sigma)$	$\Psi_{el}(\Lambda=0)=^1\Theta_{0,0}/\sqrt{2}$
$^3\Sigma_u^+(\sigma\sigma)$	$\Psi_{el}(\Lambda=0)=^3\Theta_{0,0}/\sqrt{2}$
$^1\Sigma_g^+(\pi\pi)$	$\Psi_{el}(\Lambda=0)=(^1\Theta_{1,-1}+^1\Theta_{-1,1})/2$
$^3\Sigma_u^+(\pi\pi)$	$\Psi_{el}(\Lambda=0)=(^3\Theta_{1,-1}+^3\Theta_{-1,1})/2$

wave functions [31], listed in Table I, are expressed in terms of the functions

$$^1\Theta_{\lambda,\gamma}(\Sigma=0)\equiv[P_\lambda^A(1)P_\gamma^B(2)+P_\lambda^A(2)P_\gamma^B(1)]\,^1\chi_{\Sigma=0} \tag{17}$$

and

$$^3\Theta_{\lambda,\gamma}(\Sigma)\equiv[P_\lambda^A(1)P_\gamma^B(2)-P_\lambda^A(2)P_\gamma^B(1)]\,^3\chi_{\Sigma=0,\pm1}\ , \tag{18}$$

where $\Lambda=\lambda+\gamma$.

The wave functions of Table I can be used to calculate the electrostatic quadrupole-quadrupole interaction energy between two Na ($3\,^2P$) atoms, valid at long range, for the different molecular states. The diagonal interaction energy is

$$\begin{aligned}V_{P+P}(R)&=\langle\Psi_{el}|H_{el}|\Psi_{el}\rangle\\&=\langle\Psi_{el}|V_{22}(A,B)|\Psi_{el}\rangle/R^5\equiv C_5/R^5\ ,\end{aligned} \tag{19}$$

where $V_{22}(A,B)$ is the quadrupole-quadrupole term of the multipolar expansion of the electrostatic interaction between the $3P$ electrons on atoms A and B. Equation (19) can be evaluated with the aid of the following expression [31]:

$$\begin{aligned}&\langle{}^\alpha\Theta_{\lambda,\gamma}|V_{22}(A,B)|{}^\beta\Theta_{\lambda',\gamma'}\rangle\\&\quad=2\delta_{\alpha,\beta}[\{Q_2^2(\rho_A)Q_2^{-2}(\rho_B)+Q_2^{-2}(\rho_A)Q_2^2(\rho_B)\}/24\\&\qquad-2\{Q_2^1(\rho_A)Q_2^{-1}(\rho_B)+Q_2^{-1}(\rho_A)Q_2^1(\rho_B)\}/3\\&\qquad+6Q_2^0(\rho_A)Q_2^0(\rho_B)]\ ,\end{aligned} \tag{20}$$

where $\rho_A=P_\lambda^A(1)^*P_\gamma^A(1)$ and $\rho_B=P_{\lambda'}^B(2)^*P_{\gamma'}^B(2)$ are the charge distributions of atoms A and B, and the quadrupole moment tensor elements [31] Q_2 are listed in Table II, where $\langle r^2\rangle=39.0a_0^2$ is the expectation value of the square of the Na $3P$ electronic coordinate [32]. The C_5 coefficients for the states correlating to $3P+3P$ are listed in Table III as are the C_6 coefficients of the van der Waals interaction calculated by Geltman [33]. In addition, the short-range potentials, which are very difficult to calculate accurately due to the high density of electronic states, have been calculated by Henriet and Masnou-Seeuws [34].

C. Spin-orbit interaction and Hund's case (a) to case (c) transformation

The theoretical analysis of the preceding subsection was concerned with calculating long-range wave functions and potentials which were eigenfunctions and eigen-

TABLE II. Quadrupole tensor elements from Ref. [31].

ρ	$Q_2^0(\rho)$	$Q_2^1(\rho)$	$Q_2^{-1}(\rho)$	$Q_2^2(\rho)$	$Q_2^{-2}(\rho)$
$P_0^*P_0$	$12\langle r^2\rangle/30$	0	0	0	0
$P_1^*P_1$ or $P_{-1}^*P_{-1}$	$-6\langle r^2\rangle/30$	0	0	0	0
$P_0^*P_1$ or $P_{-1}^*P_0$	0	0	$18/\sqrt{2}\langle r^2\rangle/30$	0	0
$P_1^*P_0$ or $P_0^*P_{-1}$	0	$18/\sqrt{2}\langle r^2\rangle/30$	0	0	0
$P_{-1}^*P_1$	0	0	0	0	$72\langle r^2\rangle/30$
$P_1^*P_{-1}$	0	0	0	$72\langle r^2\rangle/30$	0

TABLE III. C_5 and C_6 coefficients of the doubly excited states. Asterisk denotes from Ref. [33].

State	C_5 (a.u.)	C_6 (a.u.)*
$^1\Delta_g$	365	−6303
$^3\Delta_u$	365	−6303
$^1\Pi_g$	−1460	−9134
$^3\Pi_u$	−1460	−9134
$^1\Pi_u$	0	−9134
$^3\Pi_g$	0	−9134
$^1\Sigma_u^-$	0	−7550
$^3\Sigma_g^-$	0	−7550
$^1\Sigma_g^+(\sigma\sigma)$	1460	−147
$^3\Sigma_u^+(\sigma\sigma)$	1460	−147
$^1\Sigma_g^+(\pi\pi)$	730	−7550
$^3\Sigma_u^+(\pi\pi)$	730	−7550

values of $H_{\rm el}$, respectively. These wave functions are valid in the Hund's case (a) coupling region, where $H_{\rm el} \gg V_{\rm s.o.}$, and the good quantum numbers are Λ, Σ, S, and Ω. The analysis must now be modified to account for the spin-orbit splitting of the ^2P level into $^2P_{3/2}$ and $^2P_{1/2}$ sublevels, separated by 17.2 cm^{-1}, where the subscripts $j=3/2$ and $1/2$ denote the two ways of vectorally adding the orbital ($l=1$) and spin ($s=1/2$) angular momentum (the ground ^2S state is not split by $V_{\rm s.o.}$ because $l=0$). When the spin-orbit interaction is included, the intermediate electronic states correlate to either $\mathrm{Na}(^2S_{1/2})+\mathrm{Na}(^2P_{1/2})$ or $\mathrm{Na}(^2S_{1/2})+\mathrm{Na}(^2P_{3/2})$, and the doubly excited states correlate to either $\mathrm{Na}(^2P_{1/2})+\mathrm{Na}(^2P_{1/2})$, $\mathrm{Na}(^2P_{1/2})+\mathrm{Na}(^2P_{3/2})$, or $\mathrm{Na}(^2P_{3/2})+\mathrm{Na}(^2P_{3/2})$. For these states $H_{\rm el} \ll V_{\rm s.o.}$ at large separation, which is Hund's case (c) coupling regime, and the only good quantum number is Ω, the projection of the total angular momentum on the molecular axis.

The case (a) to case (c) transformation—as well as the case (c) potentials—are found by diagonalizing $H_{\rm el}+V_{\rm s.o.}$ expanded in the case (a) basis: the transformation matrix is the eigenvectors and the potentials are the eigenvalues. $V_{\rm s.o.}$ is taken to be R independent and of the form

$$V_{\rm s.o.} = A(\boldsymbol{l}_1\cdot\mathbf{s}_1+\boldsymbol{l}_2\cdot\mathbf{s}_2)\ , \tag{21}$$

where $A=\frac{2}{3}\Delta E$, $\Delta E=17.2$ cm^{-1} is the Na $^2P_{3/2}$-$^2P_{1/2}$ splitting, $\boldsymbol{l}$ and $\mathbf{s}$ are the orbital and spin angular momentum operators, and the subscript 1 or 2 indicates that these operators operate on electron 1 or 2, respectively. Note that $\boldsymbol{l}\cdot\mathbf{s}$ is equivalent to $(\mathbf{j}^2-\boldsymbol{l}^2-\mathbf{s}^2)/2$, where $\mathbf{j}=\boldsymbol{l}+\mathbf{s}$ is the total angular momentum of the atom (neglecting nuclear spin). One can construct eigenstates of $\boldsymbol{l}\cdot\mathbf{s}$:

$$|l,s,j,m_j\rangle=\sum_{m_s}\sum_{m_l} C(l,s,j;m_l,m_s,m_j)|l,m_l,s,m_s\rangle\ , \tag{22}$$

such that

$$\boldsymbol{l}\cdot\mathbf{s}|l,s,j,m_j\rangle = \tfrac{1}{2}[j(j+1)-l(l+1)-s(s+1)]|l,s,j,m_j\rangle\ . \tag{23}$$

In Eq. (22), $|l,m_l,s,m_s\rangle$ are the $3S$ or $3P$ orbital wave functions with electron spin, and C is a Clebsch-Gordan coefficient. For a P state electron $l=1$, $s=\frac{1}{2}$, $j=\frac{1}{2}$ or $\frac{3}{2}$, $m_l=-1$, 0, or 1 [m_l is the same as λ and γ in Eqs. (17) and (18)], and $m_s=-\frac{1}{2}$ or $\frac{1}{2}$.

Using Eqs. (22) and (23) the following spin-orbit matrix elements coupling intermediate states can be derived [28]:

$$\langle\Psi_{\rm el}(S'=1,\Lambda',\Sigma',\alpha'=g(u))|V_{\rm s.o.}|\Psi_{\rm el}(S=1,\Lambda,\Sigma,\alpha=g(u))\rangle$$
$$=(A/2)[\Lambda\delta_{\Lambda',\Lambda}\Sigma\delta_{\Sigma',\Sigma}+\delta_{\Lambda',\Lambda-1}\delta_{\Sigma',\Sigma+1}+\delta_{\Lambda',\Lambda+1}\delta_{\Sigma',\Sigma-1}]\delta_{\alpha',\alpha} \tag{24}$$

and

$$\langle\Psi_{\rm el}(S'=0,\Lambda',\Sigma',\alpha'=g(u))|V_{\rm s.o.}|\Psi_{\rm el}(S=1,\Lambda,\Sigma,\alpha=g(u))\rangle$$
$$=\langle\Psi_{\rm el}(S=1,\Lambda,\Sigma,\alpha=g(u))|V_{\rm s.o.}|\Psi_{\rm el}(S'=0,\Lambda',\Sigma'=0,\alpha'=g(u))\rangle$$
$$=(A/2)[\Lambda\delta_{\Lambda',\Lambda}\delta_{0,\Sigma}+\delta_{\Lambda',\Lambda-1}\delta_{-1,\Sigma}-\delta_{\Lambda',\Lambda+1}\delta_{+1,\Sigma}]\delta_{\alpha',\alpha}\ . \tag{25}$$

The matrix elements of $V_{\rm s.o.}$ coupling the doubly excited states can be calculated using the wave functions of Table I and the following formulas also derived from Eqs. (22) and (23):

$$\langle{}^1\Theta_{i,j}(\Sigma=0)|V_{\rm s.o.}|{}^1\Theta_{i',j'}(\Sigma'=0)\rangle=0\ , \tag{26}$$

$$\langle{}^3\Theta_{\lambda',\gamma'}(\Sigma)|V_{\rm s.o.}|{}^1\Theta_{\lambda,\gamma}(\Sigma=0)\rangle=\langle{}^1\Theta_{\lambda,\gamma}(\Sigma=0)|V_{\rm s.o.}|{}^3\Theta_{\lambda',\gamma'}(\Sigma)\rangle$$
$$=A(\delta_{\lambda,\lambda'}[-\delta_{\Sigma,1}\delta_{\gamma,\gamma'+1}+\delta_{\Sigma,0}\gamma\delta_{\gamma,\gamma'}+\delta_{\Sigma,-1}\delta_{\gamma,\gamma'-1}]-\delta_{\gamma,\gamma'}[-\delta_{\Sigma,1}\delta_{\lambda,\lambda'+1}+\delta_{\Sigma,0}\lambda\delta_{\lambda,\lambda'}+\delta_{\Sigma,-1}\delta_{\lambda,\lambda'-1}])\ , \tag{27}$$

and

$$\langle {}^3\Theta_{\lambda',\gamma'}(\Sigma')|V_{\text{s.o.}}|{}^3\Theta_{\lambda,\gamma}(\Sigma)\rangle = A(\delta_{\lambda,\lambda'}[\Sigma\delta_{\Sigma,\Sigma'}\gamma\delta_{\gamma,\gamma'}+\delta_{\Sigma,\Sigma'+1}\delta_{\gamma,\gamma'-1}+\delta_{\Sigma,\Sigma'-1}\delta_{\gamma,\gamma'+1}]+\delta_{\gamma,\gamma'}[\Sigma\delta_{\Sigma,\Sigma'}\lambda\delta_{\lambda,\lambda'}+\delta_{\Sigma,\Sigma'+1}\delta_{\lambda,\lambda'-1}+\delta_{\Sigma,\Sigma'-1}\delta_{\lambda,\lambda'+1}]) . \quad (28)$$

Due to the nature of the spin-orbit interaction, only states of the same Ω are coupled, where $\Omega=\Lambda+\Sigma$ is the projection of the total (orbital plus spin) angular momentum on the molecular axis. Also, there is no coupling between gerade and ungerade states.

The long-range case (c) molecular potentials, obtained by diagonalizing the matrix with elements $\langle\Psi'_{\text{el}}|V_{\text{s.o.}}|\Psi_{\text{el}}\rangle+\langle\Psi_{\text{el}}|H_{\text{el}}|\Psi_{\text{el}}\rangle$, are plotted in Fig. 2 for the intermediate states and in Fig. 3 for the doubly excited states. These states, which are labeled by $|\Omega|$ (states with $|\Omega|\neq 1$ are doubly degenerate), the inversion symmetry (g or u), and the reflection symmetry (+ or −, $\Omega=0$ states only), will be discussed in more detail later when we propose a PAI mechanism valid at ultracold temperatures. Since S, Σ, and Λ are no longer good quantum numbers in case (c), it is more appropriate to use $\Psi_{\text{el}}(\Omega,\alpha)$ for the electronic wave functions in Eqs. (3) and (4). Note in Fig. 2 the existence of long-range intermediate bound states of 1_u and 0_g^- symmetries, which have *inner* turning points at $R>50a_0$ [35–37]. The 0_g^- long-range bound state plays a very important role in the ultracold Na PAI process, which will be discussed in more detail in Sec. III. The intermediate state potentials appearing in Fig. 2 have also been calculated by Bussery and Aubert-Frecon [36]. We also note that the effects of the exchange interaction and of dipole-dipole couplings between the doubly excited states and states correlating to $3S+4D$, have been neglected [38].

D. Nuclear kinectic-energy operator

The kinetic operator of nuclear motion can be separated into a radial term

$$T_R=\frac{-\hbar^2}{mR}\frac{\partial^2}{\partial R^2}R \quad (29)$$

and a rotational term

$$H_{\text{rot}}=(mR^2)^{-1}(\mathbf{J}-\mathbf{L}-\mathbf{S})^2 , \quad (30)$$

where m is the Na mass, and **J**, **L**, and **S** are the total (neglecting nuclear spin), electronic orbital, and electronic spin angular momentum operators, respectively.

In this study we make the simplifying approximation

$$H_{\text{rot}}\approx(mR^2)^{-1}\mathbf{J}^2 . \quad (31)$$

Strictly speaking, Eq. (31) is valid only under limited conditions: the neglected terms may cause perturbations [39,40]. Since photon absorption occurs at large R, these perturbations are probably small for the ground and intermediate states. For the doubly excited states the perturbations might be important because autoionization occurs at small R. However, the positions of the unperturbed autoionizing bound states cannot be accurately determined theoretically because the doubly excited potentials are not known accurately enough at short range. For this reason we account for shifts caused by the neglected terms by adjusting the positions of the autoionizing bound states (by changing the well depth) to reproduce the −5-GHz cutoff in the experimental PAI spectrum.

Both T_R (in the Born-Oppenheimer approximation) and H_{rot} [using Eq. (31)] are diagonal with respect to the basis functions Eqs. (3) and (4), and have matrix elements

$$\langle\psi_0(i)|T_R+H_{\text{rot}}|\psi_0(j)\rangle = \delta_{i,j}[T_R+(\hbar^2/mR^2)J(J+1)] . \quad (32)$$

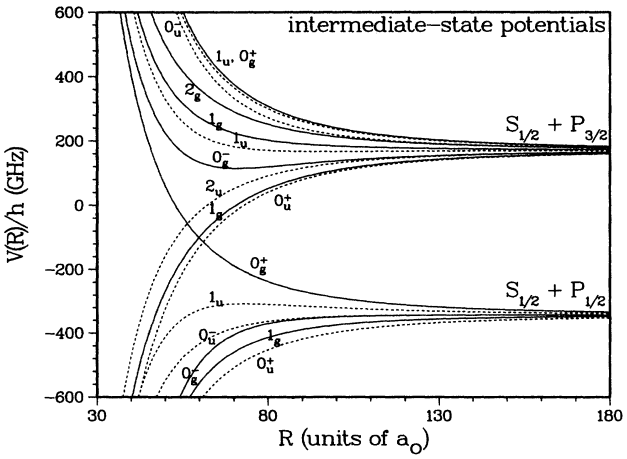

FIG. 2. Hund's case (c) long-range potentials of the intermediate states. The solid (dashed) curves correspond to states of gerade (ungerade) symmetry. The zero of energy is E_{3S+3P}.

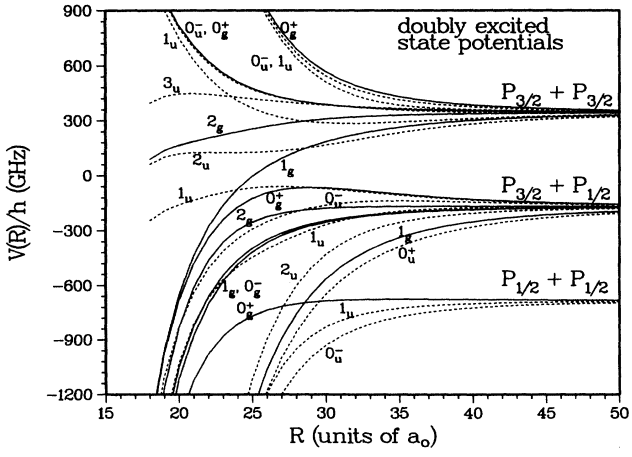

FIG. 3. Hund's case (c) long-range potentials of the doubly excited states. The solid (dashed) curves correspond to states of gerade (ungerade) symmetry. The zero of energy is E_{3P+3P}.

Note that, due to Eq. (31), J is also the rotational quantum number of bound states: the energy levels of a rigid rotor are $E_{\rm rot}=BJ(J+1)$, where B is the rotational constant.

E. Molecule-field interaction

The $H_{\rm rad}$ and $V_{\rm rad}$ terms in Eq. (2) describe the free laser field and the molecule-field interaction. The photon number states $|n\hbar\omega,\hat{\mathbf{e}}_{+1}\rangle$ in Eqs. (3) and (4) describe a laser field containing n photons of energy $\hbar\omega$ and (σ^+) polarization $\hat{\mathbf{e}}_{+1}$ and are eigenfunctions of $H_{\rm rad}=\hbar\omega a^\dagger a$, i.e., $H_{\rm rad}|n\hbar\omega,\hat{\mathbf{e}}_{+1}\rangle=n\hbar\omega|n\hbar\omega,\hat{\mathbf{e}}_{+1}\rangle$, where $a^\dagger$ and a are photon creation and annihilation operators. The molecule-field interaction in the length gauge and the dipole approximation is of the form [41]

$$V_{\rm rad}=e(8\pi\hbar\omega/cV)^{1/2}(a^\dagger+a)\hat{\mathbf{e}}_{+1}\cdot(\mathbf{r}_1+\mathbf{r}_2)\ , \tag{33}$$

where e is the electronic charge, V is the volume of quantization, and $\mathbf{r}_1$ and $\mathbf{r}_2$ are the position vectors of the unpaired electrons on Na atoms 1 and 2. $V_{\rm rad}$ has matrix elements

$$\langle\psi_0'|V_{\rm rad}|\psi_0\rangle=(8\pi\hbar\omega/cV)^{1/2}\langle n'|a^\dagger+a|n\rangle e\langle\Psi_{\rm el}'|\mathbf{r}_1+\mathbf{r}_2|\Psi_{\rm el}\rangle c(\pm,0)$$
$$\times[(2J+1)/(2J'+1)]^{1/2}C(J,1,J';M,1,M')\sum_{\mu=-1}^{1}C(J,1,J';\Omega,\mu,\Omega')\ . \tag{34}$$

The various terms in Eq. (34) are responsible for the electric dipole selection rules: $\langle n'|a^\dagger+a|n\rangle=(n+1)^{1/2}\delta_{n',n+1}+(n)^{1/2}\delta_{n',n-1}$ couples photon states differing by one photon, $e\langle\Psi_{\rm el}'|\mathbf{r}_1+\mathbf{r}_2|\Psi_{\rm el}\rangle=0$, d, or $(2)^{1/2}d$ (d is the free atom transition dipole) determines the electronic selection rules, which are $\Delta S=0$, $\Delta\Sigma=0$, $\Delta\Lambda=0,\pm1$, and $g\leftrightarrow u$, $c(\pm,0)$ is a constant which is nonzero only when ψ_0 and ψ_0' have the proper overall symmetry, and the two Clebsch-Gordan coefficients are responsible for the $\Delta J=0,\pm1$; $\Delta M=+1$; and $\Delta\Omega=0,\pm1$ selection rules.

Often it is convenient to express the molecule-field interaction in terms of the free-atom Rabi frequency $\Omega_R=2(n8\pi\omega/c\hbar V)^{1/2}d$ instead of the number of photons per volume or the electric-field strength. Note that Eq. (34) is orientation dependent, i.e., it is a function of M, the projection of the total angular momentum on the space-fixed z axis.

III. ULTRACOLD Na PHOTOASSOCIATIVE IONIZATION MECHANISM

The Na AI mechanism at normal (nonultracold) temperatures, Eq. (1), in which the atoms are resonantly excited at large separation, does not work for ultracold AI because the radiative lifetime of Na ($3P$) is much shorter than the collision time. Based on a knowledge of the long-range potentials and of the nature of the optical pumping of the free Na atoms, we propose the following mechanism for Na PAI at ultracold temperatures:

$$2\mathrm{Na}(3S)(^3\Sigma_u^+)\xrightarrow{\hbar\omega}\mathrm{Na}_2^*(0_g^-\text{ and }1_g)$$
$$\xrightarrow{\hbar\omega}\mathrm{Na}_2^{**}(1_u)\rightarrow\mathrm{Na}_2^+e^-\ , \tag{35}$$

which is illustrated in Fig. 4. We shall now explain the rationale for choosing this mechanism.

A. $^3\Sigma_u^+$ entrance channel

Although two ^2S state atoms can collide in either a $^1\Sigma_g^+$ or a $^3\Sigma_u^+$ molecular electronic state, we believe that the $^3\Sigma_u^+$ state is the entrance channel for the following reason. During each trapping phase of the optical trap the atoms interacted with a single focused beam of σ^+ polarized light [16,17]. Optical pumping with σ^+ polarized light produces Na ($3S$) in its "stretched" state, with $F=2$ and $M_F=2$ (their maximum values), where F is the total angular momentum quantum number (including nuclear spin) and M_F is its space fixed projection (in units of $\hbar$). $M_F=M_I+M_j=2$ is only possible if $M_I=\frac{3}{2}$ and $M_j=\frac{1}{2}$, their maximum values, where M_I is the space fixed projection of the nuclear spin angular momentum and $M_j\equiv M_F-M_I=M_l+M_s$ where M_l and M_s are the space fixed projection of the electronic orbital and spin angular momentum, respectively. Since $l=0$ and $M_l=0$ for S states, it follows that $M_s=M_j=\frac{1}{2}$. When two $M_s=\frac{1}{2}$ atoms collide, the space fixed projection of the total electronic spin must be $M_S=M_{s_A}+M_{s_B}=1$, which can only occur if $S=1$, i.e., if the molecule is in the $^3\Sigma_u^+$ molecular state ($S=0$ for $^1\Sigma_g^+$). Even though the space fixed projection can have only one value ($M_S=1$), there

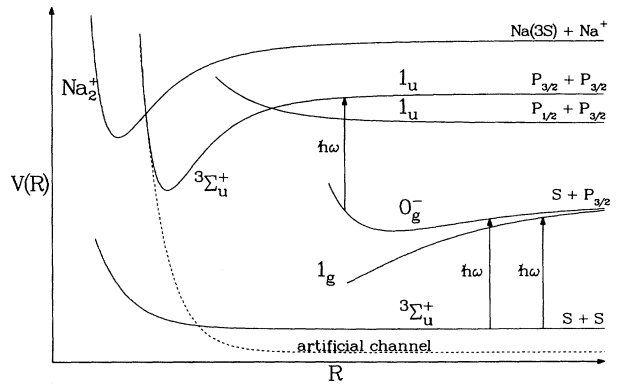

FIG. 4. Illustration of the proposed mechanism for ultracold Na PAI (not to scale). The vertical arrows denote optical transitions, and one of the doubly excited 1_u state is coupled to an artificial channel which simulates autoionization.

are three $^3\Sigma_u^+$ entrance channels because the projection of the electronic spin angular on the molecular axis can have three values, $\Sigma=0,\pm1$, because collisions can occur with any orientation with respect to the space fixed axis system.

Another consequence of the oriented spins on the collision dynamics is the disappearance of half of the rotational levels due to the nuclear statistics. Na nuclei have a spin quantum number $I=\frac{3}{2}$ and therefore obey Fermi-Dirac statistics: the total wave function $\psi_{\text{total}}=\psi_{\text{vib}}\psi_{\text{nuc}}\psi_{\text{rot-el}}$ must be antisymmetric with respect to the exchange of nuclei. The vibrational wave function, $\psi_{\text{vib}}=F_{ij}(R,E)$, is always symmetric with respect to exchange of the nuclei because it is a function of only the magnitude of the internuclear separation. The nuclear wave function ψ_{nuc} is symmetric because the nuclei have been optically pumped into the same $I=\frac{3}{2}$, $M_I=\frac{3}{2}$ spin state. The exchange symmetry of the product of the rotational and electronic wave functions $\psi_{\text{rot-el}}$ must therefore be antisymmetric. The basis functions in Eqs. (3) and (4) represent rotational-electronic wave functions with well characterized symmetry properties. For the $^3\Sigma_u^+$ electronic state the basis functions ψ_0^+ and ψ_0^0 in Eqs. (3) and (4) are symmetric with respect to exchange of the nuclei for even J and antisymmetric for odd J; whereas the basis function ψ_0^- in Eq. (3) is antisymmetric for even J and symmetric for odd J. As a result, the entrance channel corresponds to either ψ_0^+ or ψ_0^0 if J is odd, or ψ_0^- if J is even.

In the close-coupling calculation we use a spline fit to the points calculated by Konowalow, Rosenkrantz, and Olson [26] for the $^3\Sigma_u^+$ potential energy $V_{^3\Sigma_u^+}(R)$, at small separation, and an attractive van der Waals interaction with $C_6=-1698$ a.u. at large separation [36]. This potential is essentially flat in the region where photon absorption occurs.

B. 0_g^- and 1_g intermediate states

Since the trap laser is detuned slightly to the red of the $\text{Na}(3\,^2S_{1/2})\rightarrow\text{Na}(3\,^2P_{3/2})$ transition, the intermediate states must be attractive and correlate to $^2S_{1/2}+^2P_{3/2}$ at large separation in order to be on resonance with the red detuned laser frequency. The detunings of interest here ($|\Delta|>0.5$ GHz) are sufficiently large that excitation occurs at small enough separation for the electric dipole selection rules to be valid. Due to the $u\leftrightarrow g$ dipole selection rule the intermediate state must be of gerade (g) symmetry because the ground state was of ungerade (u) symmetry. In Fig. 2 one sees that one state each of 0_g^- and 1_g symmetry satisfy these requirements. The 0_g^- state is a pure long-range bound state [35–37] which is formed by an avoided crossing of a repulsive state correlating to $^2S_{1/2}+^2P_{1/2}$ and an attractive state correlating to $^2S_{1/2}+^2P_{3/2}$. It is bound by about 2 cm^{-1} and has an inner turning point at $R=55a_0$. The 1_g state is more attractive than the 0_g^- state, correlates to the chemically bound $^1\Pi_g$ state at small separation, and although it is believed not to be on resonance with a doubly excited state that leads to AI, it plays an important role in the mechanism because—depending on the value of Σ of the entrance channel—it can divert flux from the PAI pathway.

Due to the spin-orbit interaction, at long range the 0_g^- intermediate state consists of 34% $^3\Pi_g(S=1\ ,\ \Lambda=\pm1,\ \Sigma=\mp1)$ and 66% $^3\Sigma_g^+(S=1,\ \Lambda=0,\ \Sigma=0)$, and therefore is more strongly coupled radiatively to the $\Sigma=0$ (ψ_0^0) entrance channel than the $\Sigma=\pm1$ ($\psi_0^\pm$) entrance channels because of the $\Delta\Sigma=0$ selection rule. On the other hand, at long range the 1_g intermediate state consists of 58% $^3\Sigma_g^+(S=1,\ \Lambda=0,\ \Sigma=\pm1)$, which is radiatively coupled to the $\Sigma=\pm1$ ($\psi_0^\pm$) entrance channels, only 2% $^3\Pi_g$ ($S=1$, $\Lambda=\pm1$, $\Sigma=0$), which is radiatively coupled to the $\Sigma=0$ (ψ_0^0) entrance channel, and 40% $^1\Pi_g$ ($S=0$, $\Lambda=\pm1$, $\Sigma=0$), which is not radiatively coupled to any of the entrance channels because of the $\Delta S=0$ selection rule. Therefore (unlike the 0_g^- state) the 1_g state, which diverts flux from the 0_g^- state, but does not lead to PAI, is strongly coupled to the $\Sigma=\pm1$ entrance channels and very weakly coupled to the $\Sigma=0$ entrance channel. This difference in the strengths of the radiative coupling between the entrance channels and the 0_g^- and 1_g intermediate states is the key to interpreting the PAI spectrum.

Also seen in Fig. 2 are two attractive states of 2_u and 0_u^+ symmetry that correlate at large separation to $^2S_{1/2}+^2P_{3/2}$. Transitions to these states from the $^3\Sigma_u^+$ entrance channels are forbidden by the electric dipole selection rules and can occur only at very long range (small detuning) where the dipole approximation breaks down. Julienne and Vigue [12] have shown that at ultracold temperatures the 2_u state makes the dominant contribution (94%) to the intermediate state fine-structure-changing cross section. However, even if the $g\leftrightarrow u$ selection rule breaks down, the 2_u and 0_u^+ states do not have any $S=1$, $\Sigma=0$ component and therefore are not coupled to the $^3\Sigma_u^+,\Sigma=0$ entrance channel, which makes the dominant contribution to the PAI cross section. For this reason we feel that intermediate-state fine-structure-changing transitions do not play an important role in the trapping phase PAI mechanism. This is in sharp contrast to Gallagher's model [11] which assumes that intermediate-state fine-structure-changing transitions decrease the PAI rate coefficient by several orders of magnitude.

Concerning the nuclear statistics, only 0_g^- states with even J are antisymmetric with respect to the exchange of the nuclei, whereas for the 1_g state, which is doubly degenerate ($\Omega=\pm1$), half of the states are symmetric and half are antisymmetric for both even and odd J. The long-range potentials go as C_3/R^3 for the 0_g^- and 1_g states with $C_3=-6.48$ and -10.0 a.u., respectively [36]. At short range the 0_g^- potential is represented by a repulsive exponential, and the 1_g potential is joined to a spline fit of the $^1\Pi_g$ potential of Konowalow, Rosenkrantz, and Olson [26].

C. 1_u doubly excited state

Because the trap laser is detuned slightly to the red of the $\text{Na}\,(3\,^2S_{1/2})\rightarrow\text{Na}(3\,^2P_{3/2})$ transition, the doubly ex-

cited state must be attractive and correlate with Na $(3\,^2P_{3/2})$+Na$(3\,^2P_{3/2})$ at large separation. Also, the doubly excited state must have ungerade (u) symmetry because the intermediate state has gerade (g) symmetry. A third requirement is that the doubly excited state must correlate at small separation to a state that autoionizes. One state of 1_u symmetry (possibly) satisfies all these requirements.

Shown in Fig. 5 are the potential-energy curves of the doubly excited 1_u states, which were obtained by diagonalizing the matrix in Table IV at each R. The dashed curves were calculated using the long-rang theory of Sec. II, i.e., quadrupole-quadrupole plus van der Waals interaction, and the points connected by the solid curves were calculated by Krauss [42] using effective core potential methods with full two-electron configuration interaction (CI) [43]. Although the two sets of curves are similar in appearance, the upper three curves calculated using the long-range theory correlate at small separation to different case (a) states than do the curves calculated using the CI theory, because the latter accounts for the exchange interaction which is important at $R<22$ a.u. The CI theory predicts the existence of an attractive 1_u state that correlates to $P_{3/2}+P_{3/2}$ at long range, passes through and avoided crossing at $R=22a_0$ to a state that correlates at short range to a state of $^3\Sigma_u^+(\sigma\sigma)$ symmetry, which on the basis of high temperature experiments [21,22] and theoretical calculations [19] is believed to autoionize with fairly high probability. However, we stress that these curves are of only qualitative value and more accurate calculations are needed in order to put the theory on a more quantitative footing.

The long-range theory also predicts the existence of an attractive 2_u state, shown in Fig. 3, which correlates to $P_{3/2}+P_{3/2}$, but this state is inaccessible from the 0_g^- intermediate state because it violates the case (c) dipole selection rule $\Delta\Omega=0,\pm1$, and it does not correlate at small separation with a state that autoionizes at low temperature.

Due to the uncertainty concerning the exact doubly excited-state potentials, we use in most of our calculations a single attractive 1_u potential which is taken to be of the form

$$V_{1_u}(R)=4\varepsilon[(\sigma/R)^{10}-(\sigma/R)^5]+E_{P_{3/2}+P_{3/2}}\,, \tag{36}$$

where $E_{P_{3/2}+P_{3/2}}$ is the asymptotic energy, ε is the well depth, and σ is related to ε and the C_5 coefficient by

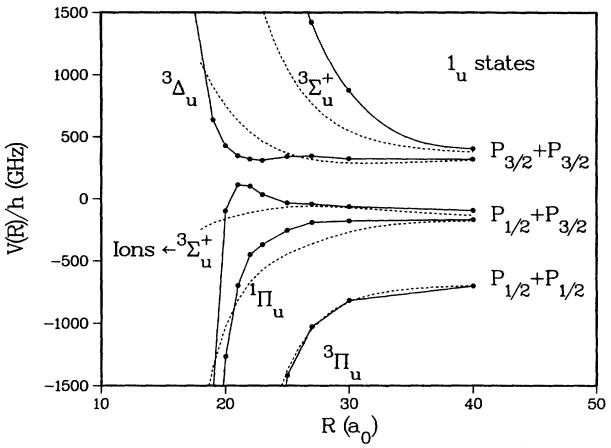

FIG. 5. The 1_u doubly excited state potentials from the full CI calculation of Krauss (points connected by solid curves), along with those calculated using long-range theory (dashed curves). The term symbols indicate the Hund's case (a) states with which the potentials correlate at small separation. Note the avoided crossing of an attractive curve correlating at long range to $P_{3/2}+P_{3/2}$ and a repulsive curve correlating to $P_{1/2}+P_{3/2}$. The zero of energy is E_{3P+3P}.

$\sigma=(-C_5/4\varepsilon)^{1/5}$. The spacing of the vibrational levels near the dissociation threshold is determined by the long-range part of the potential [44], which in turn is determined by its C_5 coefficient. C_5 is taken to be $-e^2\langle r^2\rangle^2 12/25=-730$ a.u. for most calculations, although we perform one calculation with $C_5=-430$ a.u. to determine how varying the long-range 1_u potential affects the PAI spectrum. The positions of the 1_u vibrational levels can be altered by changing the well depth ε: the choice $\varepsilon=0.0353$ a.u. (along with $C_5=-730$ a.u.) results in vibrational levels being located 20.5, 9, and 2.7 GHz below the dissociation threshold. The 9-GHz vibrational level is responsible for the cutoff in the calculated PAI spectrum at -5-GHz detuning (-9 GHz divided by two photons, plus width).

In one of the calculations of the PAI spectrum the effect of the 1_u avoided crossing (shown in Fig. 5) is investigated by including a second 1_u state which is repulsive and correlates to $P_{1/2}+P_{3/2}$ at long range. This state's potential is chosen to be of the form

TABLE IV. $H_{el}+V_{s.o.}$ matrix of the doubly excited 1_u states.

	$^3\Delta_u$	$^3\Pi_u$	$^1\Pi_u$	$^3\Sigma_u^+(\sigma\sigma)$	$^3\Sigma_u^+(\pi\pi)$
$^3\Delta_u$	$V_{^3\Delta_u}(R)-A$	$A/\sqrt{2}$	$-A/\sqrt{2}$	0	0
$^3\Pi_u$	$A/\sqrt{2}$	$V_{^3\Pi_u}(R)$	$A/2$	$A/\sqrt{2}$	$A/2$
$^1\Pi_u$	$-A/\sqrt{2}$	$A/2$	$V_{^1\Pi_u}(R)$	$-A/\sqrt{2}$	$A/2$
$^3\Sigma_u^+(\sigma\sigma)$	0	$A/\sqrt{2}$	$-A/\sqrt{2}$	$V_{^3\Sigma_u^+(\sigma\sigma)}(R)$	0
$^3\Sigma_u^+(\pi\pi)$	0	$A/2$	$A/2$	0	$V_{^3\Sigma_u^+(\pi\pi)}(R)$

$$V_{1_u'}(R)=\exp[-0.928(R-22.3)]+E_{P_{1/2}+P_{3/2}}\ , \quad (37)$$

in a.u., where $E_{P_{1/2}+P_{3/2}}$ is the asymptotic energy, and the coupling between this state and the attractive 1_u state is taken to be

$$V_{1_u,1_u'}(R)=1.75\times10^{-5}\exp[-0.025(R-32.8)^2]\ , \quad (38)$$

also in a.u. The parameters of the repulsive potential and the coupling term were chosen so that the energy at which the curve crossing occurs (but not the distance), the difference in the slopes of the potentials and the magnitude of the coupling at the crossing are similar to those predicted by the calculation of Krauss, for which Landau-Zener theory [45] predicts that about a third of the flux will jump the gap.

The 1_u avoided crossing can cause a fine-structure-changing transition and therefore represents a trap loss mechanism, because the increase in kinetic energy, equal to the $^2P_{3/2}$-$^2P_{1/2}$ splitting, is greater than the depth of the trap. The rate coefficient for the fine-structure-changing transition probably is comparable in magnitude to the PAI rate coefficient because they share the same excitation pathway.

The attractive 1_u state correlating to $P_{3/2}+P_{3/2}$ is strongly coupled radiatively to the 0_g^- state: at the inner turning point of the long-range 0_g^- state ($R=60a_0$) where the transition to the doubly excited 1_u state occurs, the 0_g^- state consists of 88% $^3\Pi_g$ ($S=1$, $\Lambda=\pm1$, $\Sigma=\mp1$) and 12% $^3\Sigma_g^+$ ($S=1$, $\Lambda=0$, $\Sigma=0$) and the doubly excited 1_u state consists of 2% $^3\Delta_u$ ($S=1$, $\Lambda=\pm2$, $\Sigma=\mp1$), 51% $^3\Pi_u$ ($S=1$, $\Lambda=\pm1$, $\Sigma=0$), and 28% $^3\Sigma_u^+$ ($S=1$, $\Lambda=0$, $\Sigma=\pm1$), which are optically coupled to the 0_g^- state, and 10% $^1\Pi_u$ and 9% $^3\Sigma_u^+$, which are not optically coupled. We mentioned earlier that the 1_g intermediate state becomes chemically bound at small separation and, at least for red detunings, never comes on resonance with the 1_u state. This may not be true for a two color red plus blue experiment, however. As with the 1_g intermediate state, half of the 1_u rotational-electronic states are symmetric and half are antisymmetric with respect to the exchange of the nuclei for both even and odd J.

D. Autoionization step

One of the greatest difficulties in formulating a complete theory of ultracold Na PAI is the inclusion of the autoionization step [21]. The proper scattering theory description is one of the incoming Na atoms and photons reacting to form outgoing Na_2^+ ions and electrons. However, due to the difficulties involved in performing *reactive* scattering calculations several approximate methods have been developed, such as the complex potential method [21,46–48] and the multichannel quantum-defect method [21,49].

In this study we treat the autoionization step by a different method, namely by coupling each doubly excited 1_u rotational-electronic state to an artificial channel, such as the one shown in Fig. 4, which are energetically open at large separation. These artificial channels simulate ionization by diverting flux from the outgoing neutral channels. The potential-energy functions for the artificial channels are chosen to intersect the 1_u potential at its inner turning point and are of the form

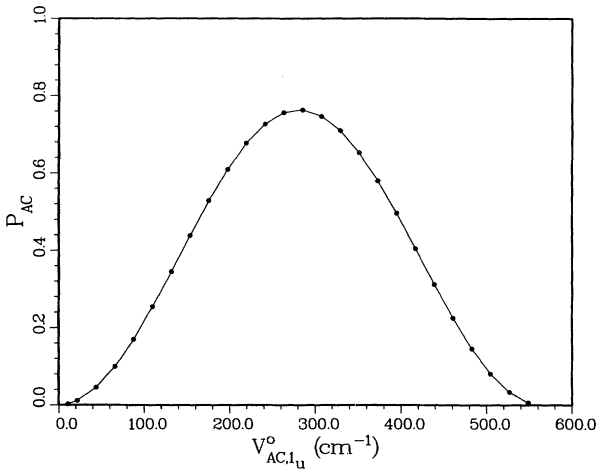

FIG. 6. The probability of crossing from the 1_u state to the artificial channel P_{AC} vs the artificial channel -1_u coupling strength $V^0_{AC,1_u}$.

$$V_{AC}(R,J'')=\exp[-3.75(R-\sigma+0.86)] -0.04+J''(J''+1)/mR^2\ , \quad (39)$$

in a.u., where σ is the same as in Eq. (37) and $J''(J''+1)/mR^2$ is a centrifugal potential.

The coupling between the 1_u state and artificial channels is taken to be

$$V_{AC,1_u}(R)=V^0_{AC,1_u}\exp[-(R-\sigma)^2]\ , \quad (40)$$

where $V^0_{AC,1_u}$ is the coupling strength at the curve crossing. The probability P_{AC} of making a transition from the 1_u state to the artificial channel is plotted as a function of $V^0_{AC,1_u}$ in Fig. 6. Not only does $V_{AC,1_u}(R)$ control the probability of making a transition from the 1_u state to the artificial channel, it also shifts and broadens the 1_u bound states as would autoionization. The choice of magnitude of $V^0_{AC,1_u}$ can be estimated from the isotropic cross sections measured at high temperature [20–22] which are in the range $\sigma=1$–4 Å^2. A choice of $J_{max}=85$, based on the potentials calculated by Dulieu, Giusti-Suzor, and Masnou-Seeuws [19], suggests that $V^0_{AC,1_u}$ should be chosen such that P_{AC} is in the range 0.15–0.6. The theoretical value of the high-temperature cross section [19] 5 Å^2, corresponds to $P_{AC}=0.75$. One of the things that we investigate in the next section is how the magnitude of $V^0_{AC,1u}$ affects the PAI spectrum.

IV. PHOTOASSOCIATIVE IONIZATION SPECTRUM

A. PAI rate coefficient

What we refer to as the PAI spectrum is the PAI rate coefficient K_{PAI} plotted as a function of the laser detun-

ing Δ from the $Na(3\,^2S_{1/2}) \rightarrow Na(3\,^2P_{3/2})$ resonance frequency. K_{PAI}, which is related to the AI rate by

$$\frac{d[Na_2^+]}{dt} = K_{PAI}[Na(3S)]^2 , \tag{41}$$

where $[Na_2^+]$ and $[Na(3S)]$ are the densities of molecular ions and ground-state atoms, respectively, is related to the T-matrix elements connecting the entrance channels (EC) and artificial channels (AC) by

$$K_{PAI} = (v\pi/3k^2)\sum_{\beta}\sum_{J}\sum_{M}\sum_{J''}|T_{EC,AC}(\beta,J,M,J'')|^2 , \tag{42}$$

where v is the collision velocity, which is related to the wave vector $k=(mE/\hbar^2)^{1/2}$ by $v=2\hbar k/m$, and the T-matrix elements are labeled by the entrance channel $\beta=\psi_0^+$, ψ_0^0, or ψ_0^-, the total angular momentum of the entrance channel J, its space fixed projection M ($M=-J,-J+1,\ldots,J$), and the total angular momentum of the artificial channel J'' ($M''=M+2$). The 3 in the denominator is due to the threefold degeneracy of the entrance channels, and only odd J contribute to the sum for ψ_0^+ and ψ_0^0 entrance channels and only even J for the ψ_0^- entrance channel, due to the nuclear statistics. This corresponds to summing over only even values of the orbital quantum number l, where $l=J\pm1$ for the ψ_0^+ and ψ_0^0 entrance channels and $l=J$ for the ψ_0^- entrance channel.

The T-matrix elements are obtained by solving the coupled equations [Eq. (6)] for $F_{ji}(R,E)$, using the Gordon algorithm [50] subject to the boundary conditions (in matrix form)

$$\mathbf{F}(R,E)=0 \tag{43}$$

as $R\rightarrow 0$ and

$$\mathbf{F}(R,E)=\mathbf{J}(R)\,\mathbf{A}-\mathbf{N}(R)\mathbf{B} \tag{44}$$

as $R\rightarrow\infty$, where $\mathbf{J}(R)$ and $\mathbf{N}(R)$ are diagonal matrices related to the spherical Bessel functions of the first and second kinds [51], and $\mathbf{A}$ and $\mathbf{B}$, which are determined by the calculation, are related to the T matrix by [51]

$$\mathbf{T}=-2i\mathbf{B}\mathbf{A}^{-1}(\mathbf{1}-i\mathbf{B}\mathbf{A}^{-1})^{-1} , \tag{45}$$

where $\mathbf{1}$ is the unit matrix.

B. Simplifications of the model

Even though a large fraction of the Na_2, Na_2^*, and Na_2^{**} electronic states have been eliminated due to our choice of mechanism, additional simplifications can be realized—this time with regard to the rotational (orbital) motion of the colliding atoms. This is accomplished by neglecting rotational branching due to optical pumping of the $Na_2\rightarrow Na_2^*$ rovibronic transition, by using an orientation averaged molecule-field interaction, and by developing a model based on $\Delta J=0$ rather than $\Delta J=0,\pm1$ selection rules.

In most of the calculations that follow, we neglect optical pumping effects and adopt what we call an "up-only" level structure, which is illustrated in Fig. 7(a) for the

$$Na_2(^3\Sigma_u^+;\beta,J,M,n\hbar\omega) \rightarrow Na_2^*(0_g^-;\beta',J',M+1,(n-1)\hbar\omega) \rightarrow Na_2^{**}(1_u;\beta'',J'',M+2,(n-2)\hbar\omega) \tag{46}$$

excitation pathway. This pathway corresponds to the odd J, $\beta=\psi_0^0$ entrance channel, which is very weakly coupled to the 1_g state. For the odd J, $\beta=\psi_0^+$ entrance channel one must include the transition

$$Na_2(^3\Sigma_u^+;\beta,J,M,n\hbar\omega)\rightarrow Na_2^*(1_g;\beta',J',M+1,(n-1)\hbar\omega) \tag{47}$$

in the excitation pathway, with $J'=J,J\pm1$. The pathway for the even J, $\beta=\psi_0^-$ entrance channel includes both Eqs. (46) and (47), but with $J'=J$ for the 0_g^- state and $J''=J,J\pm1$ for the 1_u state. In all cases each 1_u rotational level J'' is coupled to an artificial channel.

One can include the effects of optical pumping by including additional excitation pathways such as those

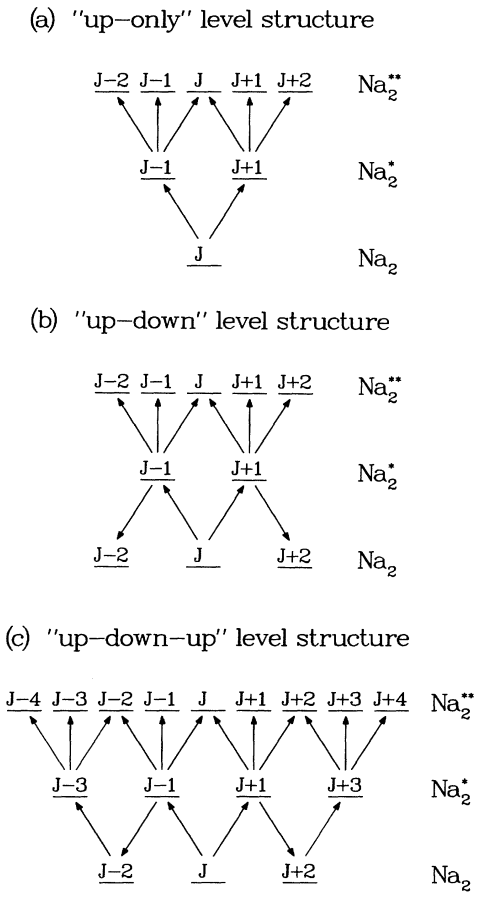

FIG. 7. Level structure used in the calculations. (a) The "up-only" level structure is used to calculate all of the AI spectra. (b) The "up-down" and (c) "up-down-up" level structures contain additional rotational levels to account for the effects of optical pumping of the $Na_2\rightarrow Na_2^*$ rovibronic transition.

shown in Figs. 7(b) and 7(c). We refer to these as "up-down" and "up-down-up" level structures. Normally one would keep adding levels until the T-matrix element converges [52]. However, this approach quickly becomes computationally prohibitive because the computational effort scales as N^3 where N is the number of levels, i.e., the number of terms in the wave-function expansion [Eq. (5)]. In the next section we show that optical pumping leads to a broadening of the PAI spectrum, which can be simulated by convolving the spectrum, calculated using the up-only level structure, with a narrow Lorentzian.

If the atomic motion in the trap is isotropic, then during the collision the molecular axis can have any orientation with respect to the electric-field vector. This is manifested in the rate coefficient expression [Eq. (42)] as a sum over M-dependent T-matrix elements. The M dependence of the T-matrix elements arises from the M-dependent Clebsch-Gordan coefficient $C(J,1,J';M,1,M'=M+1)$ in the molecule-field coupling term, Eq. (34). We refer to the coupled equations with the M-dependent interaction as the *orientation-dependent model.*

As suggested by Peploski and Eno [53], the orientation dependence of the molecule-field interaction can be removed by substituting for $C(J,1,J';M,1,M+1)$ its root-mean-square average times a phase factor:

$$\overline{C(J,1,J';M,1,M+1)}=\left[\sum_{M=-J}^{J} C(J,1,J';M,1,M+1)^2\right]^{1/2}/(2J+1)^{1/2}(-1)^{(|J-J'|+J+J')} \tag{48}$$

for the $Na_2(J,M)\rightarrow Na_2^*(J',M+1)$ transition and

$$\overline{C(J',1,J'';M+1,1,M+2)}=\left[\sum_{M=-J}^{J} C(J,1,J'M,1,M+1)^2 C(J',1,J'';M+1,1,M+2)^2\right] \times\left[\left[\sum_{M=-J}^{J} C(J,1,J';M,1,M+1)^2\right]^{1/2}(-1)^{(|J''-J'|+J'+J'')}\right]^{-1} \tag{49}$$

for the $Na_2^*(J',M+1)\rightarrow Na_2^{**}(J'',M+2)$ transition. Equation (49) has this particular form to ensure that the product of Eqs. (48) and (49) equals the root-mean-square average of $C(J,1,J';M,1,M+1)C(J',1,J'';M+1,1,M+2)$, times a phase factor. Using Eqs. (48) and (49) in the coupled equations results in an M-independent T matrix, one can express the rate coefficient expression as

$$K_{\mathrm{PAI}}=(v\pi/3k^2)\sum_{\beta}\sum_{J}\sum_{J''}(2J+1)|T_{\mathrm{EC,AC}}(\beta,J,J'')|^2 . \tag{50}$$

A very sizable reduction of computational effort is realized by this approximation because the coupled equations are solved only once per J (per detuning) rather than $2J+1$ times per J (per detuning), with $J_{\max}=10$ in our case. We refer to this approximation as the *orientation-independent model.*

The orientation-independent model can be simplified even further by replacing *all* Clebsch-Gordan coefficients by their root-sum-square value [54], e.g.,

$$\bar{C}=\left[\sum_{J'} C(J,1,J',M,1,M+1)^2\right]^{1/2}=1 . \tag{51}$$

This results in $J''=J'=J$ and a J''- and M-independent T matrix, and the rate coefficient expression reduces to

$$K_{\mathrm{PAI}}=(v\pi/3k^2)\sum_{\beta}\sum_{J}(2J+1)|T_{\mathrm{EC,AC}}(\beta,J)|^2 . \tag{52}$$

In our case this approximation reduces the dimensionality N of the coupled equations by up to a factor of 3. This is probably a good approximation, at least for the absorption of the first photon which occurs at long range, because the rotational constant and hence the rotational spacings are small. We find that a better approximation is to sum Eq. (52) over both odd and even J for all three entrance channels β and then divide K_{PAI} by 2. We call this approximation the *orientation- and J', J''-independent model.*

In the next part of this section we test these orientation averaging and level-structure approximations. In all calculations we use an orientation- and J'-independent approximation for the $Na_2(^3\Sigma_u^+)\rightarrow Na_2^*(1_g)$ transition, namely we use Eq. (51) in the matrix element coupling these states, and we also assume that $J'=J$.

C. Entrance channel effects and the role of bound-state structure

Shown in Fig. 8(a) is the PAI spectrum calculated using the orientation-dependent model and the up-only level structure. The electric-field strength is chosen to correspond to a free-atom Rabi frequency of $\Omega_R/2\pi=1.5$ GHz, which is similar to the experimental conditions of Lett *et al.* [16], and the collision energy is $E/k_B=0.75$ mK. The parameters of the 1_u potential were chosen so that one of the vibrational levels lies 9 GHz below the dissociation threshold. The artificial-channel–1_u coupling strength is $V^0_{\mathrm{AC},1_u}=123\ \mathrm{cm}^{-1}$, which corresponds to $P_{\mathrm{AC}}=0.3$, and the PAI rate coefficient is calculated at detuning intervals of 0.0125 GHz, with $J=1-10$ contributing.

Resonance structure, consisting of five broad peaks and numerous narrow peaks, is clearly evident in Fig. 8(a). In Figs. 8(b) and 8(c) the PAI spectrum is separated into contributions from odd and even initial J. Figure 8(b)

shows that the odd J (ψ_0^+ and ψ_0^0) entrance channels make the largest contribution to the PAI spectrum. The broad peaks occur at detunings that are two-photon resonant with the lower rotational levels of the 1_u vibrational level lying 9 GHz below the dissociation threshold and the largest peaks occur at detunings that are also one-photon resonant with the 0_g^- vibrational levels. The positions of the lower rotational levels of the 1_u vibrational level lying 9 GHz below the dissociation threshold, and the field free 0_g^- vibrational levels, are indicated in Figs. 8(b) and 8(c), respectively. In Fig. 8(c) one sees that the even J (ψ_0^-) entrance channels make a much smaller contribution to the PAI spectrum, and clusters of narrow peaks occur at detunings that are resonant with the 0_g^- vibrational levels.

The PAI spectra shown in Fig. 8 can be explained with the help of the "field dressed" potentials shown in Fig. 9. These potentials are the R dependent eigenvalues of $H_{\rm el}+V_{\rm s.o.}+H_{\rm rad}+V_{\rm rad}$, and were calculated using a large detuning ($\Delta=-10$ GHz) to aid visualization. We make the approximation, valid for $|\Delta|>1$ GHz, that all the incoming flux is in the $\bar{S}+\bar{S}$ channel (the bar denotes field dressed state). The collision energy ($E/h=0.016$ GHz) is very slightly above the $\bar{S}+\bar{S}$ asymptote, and the curves that would correspond to $S+P$ and $P+P$ at small field strength have been shifted down by $\hbar\omega$ and $2\hbar\omega$, respectively, because the photon states associated with these states have one and two fewer photons. Note that the $\bar{S}+\bar{S}$, $\bar{S}+\bar{P}$, and $\bar{P}+\bar{P}$ potentials shift with respect to each other when the detuning is changed. The avoided

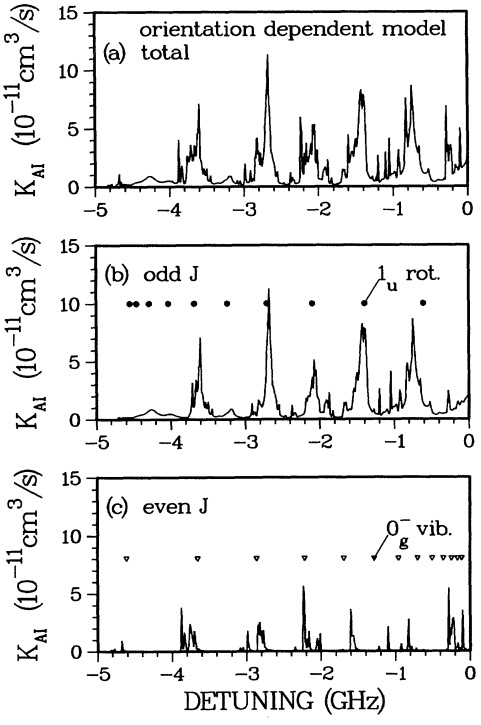

FIG. 8. The PAI spectrum (rate coefficient vs laser detuning) calculated using the orientation-dependent model. (a) The total spectrum is separated into contributions from (b) odd J (ψ_0^0 and ψ_0^+) and (c) even J (ψ_0^-) entrance channels.

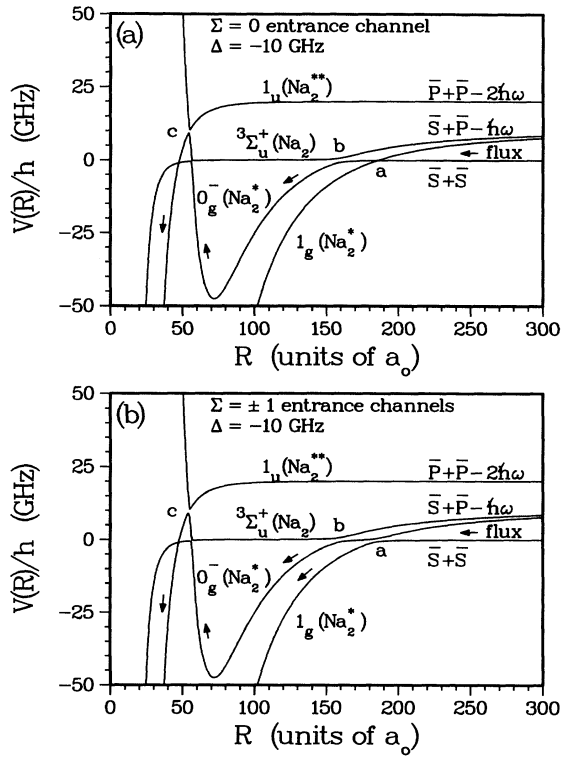

FIG. 9. Potential-energy curves of the field-dressed states corresponding to radiative couplings appropriate for (a) the $\Sigma=0$ (ψ_0^0) entrance channel and (b) the $\Sigma=\pm1$ (ψ_0^+ and ψ_0^-) entrance channel.

crossings labeled a, b, and c are due to the $^3\Sigma_u^+\rightarrow1_g$, $^3\Sigma_u^+\rightarrow0_g^-$, and $0_g^-\rightarrow1_u$ radiative transitions, respectively, and occur at separations where the energy difference between the field free potentials equals the photon energy. The curves shown in Fig. 9(a) correspond to radiative couplings appropriate for a $\Sigma=0$ (ψ_0^0) entrance channel and those in Fig. 9(b) to radiative couplings appropriate for $\Sigma=\pm1$ (ψ_0^+ and ψ_0^-) entrance channels.

In Fig. 9(a), incoming flux (denoted by arrows) bypasses avoided crossing a due to the weak coupling between the 1_g state and the $\Sigma=0$ component of the $^3\Sigma_u^+$ state. Flux passes adiabatically through avoided crossing b due to the small difference in slopes of the field free potentials and the strong radiative coupling, and is either reflected at or passes through the avoided crossing c. The probability of making it past c is less than for making it past b because the difference in the 0_g^- and 1_u slopes is greater. Flux that makes it past c can reach the inner turning point of the 1_u potential where it can jump to the artificial channel with probability $P_{\rm AC}=0.3$. Since the probability of passing through c is enhanced if the incident energy is resonant with a 1_u field dressed bound states, peaks are seen in the PAI spectrum whenever the detuning is two-photon resonant with 1_u rotational levels corresponding to the vibrational level lying 9 GHz below the dissociation threshold. Due to our choice of large detuning (-10 GHz), the avoided crossing c lies well above the incident energy and flux must tunnel through the bar-

rier for PAI to occur: the degree of attractiveness of the 1_u state plays an important role in determining the cutoff of the PAI spectrum. Features due to higher rotational levels (higher J'') of the 1_u vibrational level lying 20.5 GHz below the dissociation threshold do not appear in the spectrum because the centrifugal barrier in the entrance channel is too large for high J. Peaks corresponding to the lower rotational levels of the 1_u vibrational level lying 2.7 GHz below the dissociation threshold make only a small contribution to the PAI spectrum because the sum over M in the rate coefficient expression tends to weight the contribution from each J by $2J+1$, and J is small.

Flux that is reflected at c travels out through b to large separation. Features due to 0_g^- vibrational levels are not seen in the PAI spectrum because flux is not efficiently trapped in the 0_g^- field dressed potential well, which is another way of saying that the widths of the 0_g^- vibrational levels are large due to power broadening. At detunings beyond about -3 GHz the 0_g^- vibrational spacing is sufficiently large compared to their widths to be able to modulate the spectrum; the peak in Fig. 8 at -3.2 GHz is much smaller than the peak at -3.7 GHz, because this wavelength is not resonant with a 0_g^- vibrational level. The 0_g^- rotational constant is much smaller than the 1_u rotational constant due to the long-range nature of the 0_g^- potential, and the 0_g^- bound states shift only slightly with J'.

The dressed state potential curves shown in Fig. 9(b) correspond to a radiative coupling appropriate for the $\Sigma=\pm1$ (ψ_0^+ and ψ_0^-) entrance channels, and are essentially the same as those in Fig. 9(a) except for the large avoided crossing a due to the strong radiative coupling between the $\Sigma=\pm1$, $^3\Sigma_u^+$ entrance channels and the 1_g state. Note the existence of a "shelf" state, which is 0_g^--like between c and b, $^3\Sigma_u^+$-like between b and a, and 1_g-like beyond a. This shelf state has a very small rotational constant because the vibrating molecule spends most of its time at the outer turning point. Also, the widths of the levels are very narrow due to the strength of the avoided crossing a. Since the colliding energy is only slightly above the shelf, the positions of the resonances are determined by the 0_g^- potential because that is where the phase of the vibrational wave function develops. One expects to see narrow peaks in the PAI spectrum because only at detunings for which the incident energy is resonant with the narrow 0_g^- levels can the flux efficiently jump the gap at a and proceed to AI.

The PAI spectrum in Fig. 8 can be interpreted with the help of the field dressed potentials shown in Fig. 9. The positions and widths of the peaks are determined by whichever is narrowest: the 1_u or 0_g^- field dressed levels, and the heights of the peaks are sensitive to the degree of overlap of the 1_u and 0_g^- levels. The widths of the 1_u levels are determined primarily by the artificial channel coupling, whereas the widths of the 0_g^- levels are determined by the radiative coupling, which depends on the entrance channel. In the even J spectrum, Fig. 8(c), which corresponds to the ψ_0^- entrance channel and the field dressed potentials of Fig. 9(b), the 0_g^- levels are narrower than the 1_u levels and one sees clusters of narrow peaks at detunings one-photon resonant with the 0_g^- levels. The different peaks in each cluster correspond to different rotational shifts, which are a function of J', and ac Stark shifts, which are a function of M. On the other hand, in the odd J spectrum, Fig. 8(b), which corresponds to the ψ_0^0 and ψ_0^+ entrance channels, the ψ_0^0 entrance channel dominates, as it does in the total PAI spectrum, because flux is not diverted at a to the 1_g state. For the ψ_0^0 entrance channel the 1_u levels are narrower than the 0_g^- levels and therefore they determine the positions and widths of the resonances.

D. Orientation averaging and optical pumping effects

Much computational effort was required to calculate the PAI spectrum shown in Fig. 8(a), using the orientation-dependent model and "up-only" level structure, which accounts for orientation averaging but not optical pumping effects. We now attempt to isolate the role of orientation averaging and optical pumping in the hope of simulating these effects while using the simpler models. In Fig. 10 the role of orientation averaging is illustrated by plotting the M-dependent PAI probability $P_{\rm PAI}(M)\equiv|T_{\rm EC,AC}(\beta=\psi_0^0,J=5,M,J''=7)|^2$ for the $J=5\rightarrow J''=7$ transition from the ψ_0^0 entrance channel, calculated using the orientation-dependent model for detunings in the range $\Delta=-1.9$ to -2.4 GHz. The M-dependent radiative interaction results in an M-dependent ac Stark shift of the bound states which shifts the individual $P_{\rm PAI}(M)$. The PAI probability calculated using the orientation-independent model is also shown (dashed curve). The orientation-independent peak, which should be multiplied by $2J+1=11$ in order to compare it with the sum over M peak, overestimates the probability for this particular transition, although the position of the peak is reasonably accurate.

Since the probability summed over M is broader than the individual $P_{\rm PAI}(M)$ and the $P_{\rm PAI}$ calculated using the orientation-independent model, we conclude that the

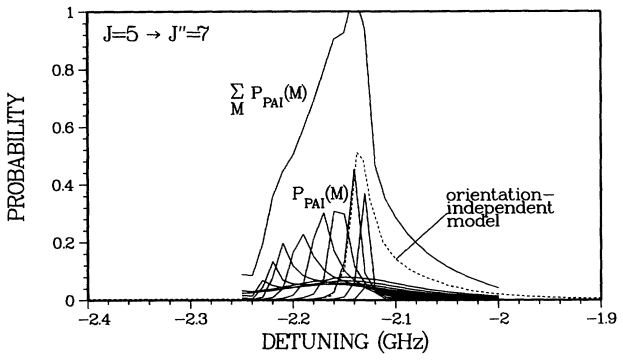

FIG. 10. The role of orientation averaging in broadening the PAI spectrum. The PAI probability $P_{\rm PAI}(M)$ vs detuning for the $J=5\rightarrow J''=7$ transition is calculated using the orientation-dependent model (solid curves) for $M=-J,-J+1,\ldots,J$, along with the probability calculated using the orientation-independent model (dashed curve).

effect of orientation averaging, i.e., summing over M, is to broaden the PAI spectrum. This conclusion is supported by Figs. 11(a) and 11(b) where the total PAI spectrum calculated using the orientation-independent model and the orientation and J',J''-independent model are plotted—the broadest features in these spectra are narrower than the broadest features in the PAI spectrum calculated using the orientation-dependent model [Fig. 8(a)]. It is pleasing to note that the spectra calculated using the different models are qualitatively similar—especially considering that $\Delta J=0$ selection rules are used in the orientation and J',J''-independent model. The ratio of computational effort associated with the three models is approximately 50:5:1.

The role of optical pumping of the $Na_2 \rightarrow Na_2^*$ transition is illustrated in Fig. 12, where $P_{PAI}(M)$ summed over M is plotted for the $J=5 \rightarrow J''=7$ transition, calculated using the orientation-dependent model and either the up-only, the up-down, or the up-down-up level structure (see Fig. 7). The peaks calculated using the up-down and up-down-up level structures are much broader than that calculated using the up-only level structure, which indicates that optical pumping is an additional source of broadening. This broadening can be simulated by convolving P_{PAI} calculated using the up-only level structure with a Lorentzian of width $\Gamma=0.1$ GHz:

$$\bar{P}_{PAI}(\Delta)=\int d\Delta' P_{PAI}(\Delta')(\Gamma/2\pi)/[(\Delta-\Delta')^2+\Gamma^2/4] \ . \tag{53}$$

This broadened peak, also shown in Fig. 12, is (perhaps fortuitously) very similar in height, width, and position to the peak calculated using the more elaborate up-down-up level structure. One must convolve the peak calculated using the orientation-independent model with a slightly

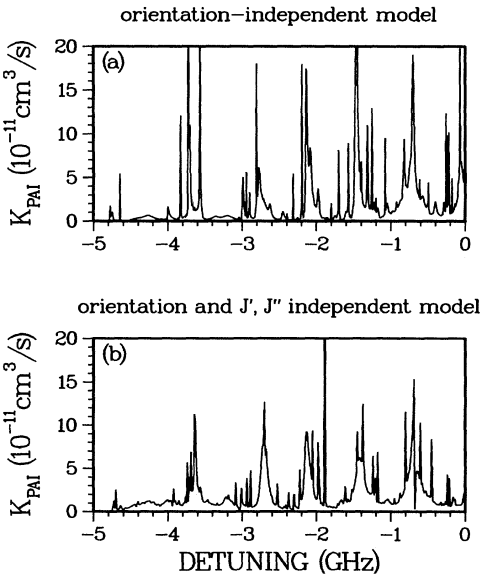

FIG. 11. PAI spectra calculated using (a) the orientation-independent model and (b) the orientation- and J',J''-independent model.

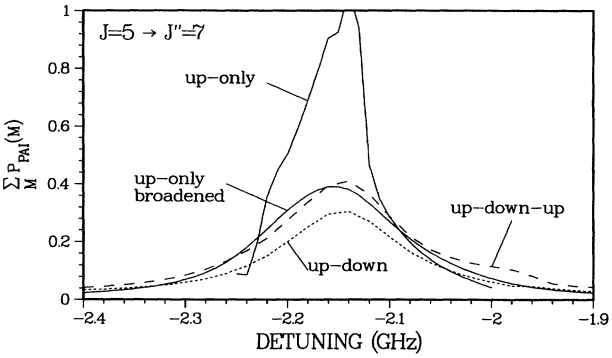

FIG. 12. The role of optical pumping of the $Na_2 \rightarrow Na_2^*$ rovibronic transition in broadening the PAI spectrum. The PAI probability summed over M vs the detuning for the $J=5 \rightarrow J''=7$ transition is calculated using the up-only (solid curve), the up-down (small-dashed curve), and the up-down-up (large-dashed curve) level structures. Also shown (solid curve) is the up-only curve that has been broadened by convolving it with a Lorentzian of width $\Gamma=0.1$ GHz.

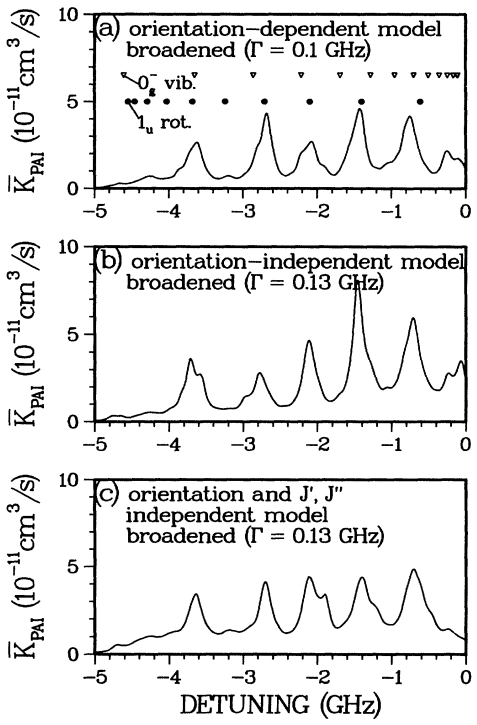

FIG. 13. Broadened PAI spectra calculated using (a) the orientation-dependent model, (b) the orientation-independent model, and (c) the orientation- and J',J''-independent model. The spectrum in (a) was obtained by convolving the spectrum in Fig. 8(a) with a Lorentzian of width $\Gamma=0.1$ GHz to account for broadening due to optical pumping. The spectra in (b) and (c) were obtained by convolving the spectra in Figs. 11(a) and 11(b) with a Lorentzian of width $\Gamma=0.13$ GHz to account for broadening due to both optical pumping and orientation averaging.

broader Lorentzian, $\Gamma=0.13$ GHz, to account for both optical pumping *and* orientation averaging.

One can also broaden the PAI spectrum in a similar manner:

$$\bar{K}_{\mathrm{PAI}}(\Delta)=\int d\Delta' K_{\mathrm{PAI}}(\Delta')(\Gamma/2\pi)/[(\Delta-\Delta')^2+\Gamma^2/4] \ . \tag{54}$$

The broadened PAI spectra, calculated using the orientation-dependent model, the orientation-independent model, and the orientation and J',J''-independent model, are shown in Fig. 13. Comparing the broadening spectra with the unbroadened spectra [Figs. 8(a), 10(a), and 10(b)] it appears that the broad "1_u rotational" peaks associated with the ψ_0^0 entrance channel survive, but the clusters of narrow "0_g^- vibrational" peaks associated with the ψ_0^+ and ψ_0^- entrance channels are either washed out or appear as bumps or shoulders on the broad peaks. Note that we have ignored broadening due to the hyperfine splitting, which is on the order of 0.1 GHz.

Each model predicts five peaks between $\Delta=-0.5$ and -4.0 GHz at essentially the same positions, and also a cutoff at $\Delta\approx-5$ GHz similar to experiment. Although there are many similarities, the resonance structure in the experimental spectrum is still broader than in our broadened spectra, and additional resonance structure is present. On a quantitative level, the calculated rate coefficient in Fig. 13(a) at the peak maximum $\Delta=-0.75$ GHz is approximately an order of magnitude greater than the experimentally determined value of $K_{\mathrm{PAI}}=2.6^{+3.0}_{-1.2}\times10^{-12}$ cm^3/s measured at $\Delta=-0.6$ GHz, which corresponds to the same maximum in the experimental PAI spectrum.

E. Sensitivity of the PAI spectrum to the parameters of the calculation

We now take advantage of the success of the broadened orientation- and J',J''-independent model in reproducing the features of the broadened orientation-dependent model calculation—at a small fraction of the computational effort—to study the sensitivity of the PAI spectrum to the parameters of the calculation.

1. *Artificial channel coupling*

The first parameter that is varied is $V^0_{\mathrm{AC},1_u}$, the coupling between the artificial channel and the 1_u state. Plotted in Fig. 14 are PAI spectra calculated using $V^0_{\mathrm{AC},1_u}=65.8$ and 171 cm^{-1}, which corresponds to $P_{\mathrm{AC}}=0.1$ (weak coupling) and 0.5 (strong coupling), respectively. These spectra, along with the one shown in Fig. 13(c) for which $P_{\mathrm{AC}}=0.3$, all display resonance structure over a range of P_{AC} similar to the uncertainty (0.15–0.6) in the experimentally determined high temperature AI probability. The 1_u levels, and therefore the resonance structure, are narrow for weak coupling, and the 1_u rotational progression is evident in Fig. 14(a). In the strong coupling example shown in Fig. 14(b), the 1_u rotational structure is less resolved and the bumps and shoulders due to the 0_g^- vibrational structure are visible. Also, the integrated spectrum, i.e., the area under the curve, is not proportional to P_{AC}.

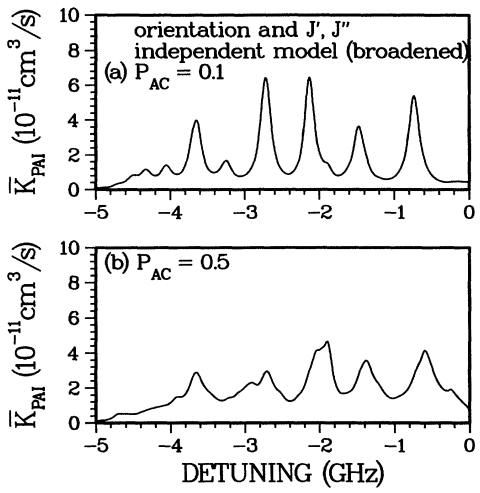

FIG. 14. Broadened ($\Gamma=0.13$ GHz) PAI spectra calculated using the orientation- and J',J''-independent model for (a) weak and (b) strong coupling between the artificial channel and the 1_u state.

2. *1_u long-range potential*

Next, the PAI spectra is calculated using a less attractive 1_u potential, with $C_5=-430$ a.u. and $\varepsilon=0.034\,27$ a.u. [see Eq. (36)], where ε has been adjusted so that there exists a 1_u vibrational level 9 GHz below the dissociation threshold, as before. The resulting spectrum, show in Fig. 15, is qualitatively similar to the spectrum in Fig. 12(c) in that there are five major peaks between $\Delta=-0.5$ and -4.0 GHz, although the positions of the peaks are slightly different because the 1_u rotational constant is different. On the other hand, the envelope of the peaks is considerably modified: the rapid falloff of the PAI rate coefficient as a function of detuning is due to the avoided crossing labeled *c* in Fig. 9 lying at energies greater than the incident energy at smaller detunings than it would for a more attractive 1_u potential.

The 1_u potential in Fig. 5 that correlates to $P_{3/2}+P_{3/2}$

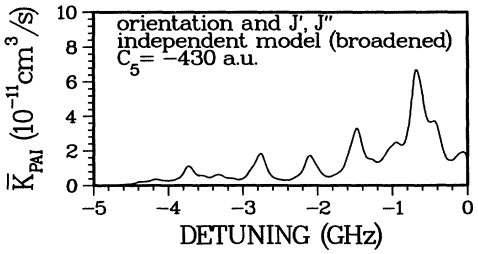

FIG. 15. Broadened ($\Gamma=0.13$ GHz) PAI spectrum calculated using the orientation and J',J''-independent model using a less attractive 1_u state with $C_5=-430$ a.u.

is less attractive than the $C_5 = -730$ and -430 a.u. potentials that have been used in the calculations of the PAI spectra so far. This appears to be in disagreement with the experimental PAI spectrum whose envelope is more similar to that of the calculations using the more attractive potential, with $C_5 = -730$ a.u.

3. 1_g bound states

Although the role of the 0_g^- and 1_u bound-state structure has been discussed, nothing has been said so far about the 1_g bound states. The 1_g bound states play an important role in the PAI mechanism because flux is more efficiently diverted from the pathway leading to PAI whenever the laser is on resonance with the field dressed bound states. The spacing of the high-lying 1_g vibrational states is determined by its C_3 coefficient [44], but the specific energies at which the levels occur are determined by the potential as a whole. The uncertainty in the short range potential, which is a fit to the $^1\Pi_g$ potential of Konowalow, Rosenkrantz, and Olson [26], is too great to determine the energies to high accuracy. The effect on the PAI spectrum of shifting the position of the 1_g vibrational levels by modifying the short-range part of the potential is shown in Fig. 16. The solid and dashed curves were calculated using the modified and unmodified potentials, respectively, and the positions of the shifted and unshifted field-free 1_g vibrational levels are also shown. Interestingly, the spectrum calculated using the modified potential displays a larger rate coefficient over almost the entire range of detunings, and especially at $\Delta = -3.6$ GHz. A $\Delta = -3.2$ GHz peak, which is seen experimentally, is also visible. The positions of the peaks, however, are relatively unchanged.

4. 1_u avoided crossing

Finally, the role of the 1_u avoided crossing seen in Fig. 5 is examined. The avoided crossing is a result of the coupling between a repulsive state correlating to $P_{1/2}+P_{3/2}$ at long range, which crosses an attractive state correlating to $P_{3/2}+P_{3/2}$ at long range and to the autoionizing $^3\Sigma_u^+$ state at short range. In the mechanism

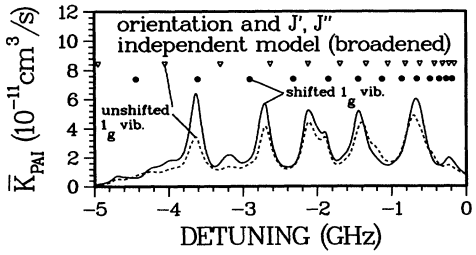

FIG. 16. Broadened ($\Gamma = 0.13$ GHz) PAI spectra calculated using the orientation and J', J''-independent model using a 1_g potential that has been modified at short range to shift the position of the 1_g vibrational levels (solid curve), along with the spectrum of Fig. 13(c) (dashed curve) corresponding to the unshifted levels. The positions of the shifted and unshifted field-free 1_g vibrational levels are also shown.

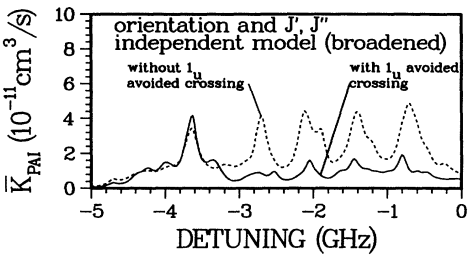

FIG. 17. Broadened ($\Gamma = 0.13$ GHz) PAI spectra calculated using the orientation and J', J''-independent model with (solid curve) and without (dashed curve) the 1_u avoided crossing.

proposed in this paper, flux must jump this gap in order for AI to occur. We model this avoided crossing by using Eqs. (36) and (37) for the attractive and repulsive 1_u potentials, and Eq. (38) for the coupling term. The parameters of the repulsive potential and coupling term were chosen to yield the same Landau-Zener curve crossing probability ($P = 0.35$) as the potentials calculated by Krauss [42] using an effective core potential method with full two-electron configuration interaction, which are also shown in Fig. 5.

The PAI spectra calculated with and without the 1_u avoided crossing are shown in Fig. 17. The addition of the 1_u avoided crossing results in significant modification of the PAI spectrum that cannot be explained in terms of Landau-Zener theory [45], and is probably due to some sort of interference effect. We find that the PAI spectrum is sensitive to the range of the coupling term, which supports this interpretation. For $|\Delta| < 3$ GHz the rate coefficient is suppressed, bringing it more in line with the experimental value, and the peaks appear as small bumps on a broad background—similar to the experimental spectrum. For $|\Delta| > 3.5$ GHz the spectrum remains essentially unmodified, except for the appearance of additional structure.

Although the envelope of the spectrum calculated with the avoided crossing is skewed toward larger detunings to a greater extent than the envelope of the experimental PAI spectrum, many similarities exist between the two spectra: both have four major peaks between -0.5 and -3 GHz, a minimum at -3 GHz, a large peak at -3.7 GHz with several smaller peaks on either side, and a cutoff at about -5 GHz. The calculated rate coefficient at -0.6-GHz detuning is too high by about a factor of 4.

V. PREDICTIONS BASED ON THE PROPOSED PAI MODEL

Based on the theory presented in the preceding sections, we can suggest several experiments to test the predictions of our PAI model. The experimental verification or lack of verification of these predictions will aid in determining the applicability of the model, and in suggesting possible improvements.

One prediction mentioned earlier concerned the production of $Na(3\,^2P_{1/2})$ as the result of the avoided crossing between two doubly excited 1_u states (see Fig. 5). A

simple Landau-Zener estimate, based on the potentials of Krauss, suggest that this fine-structure-changing transition occurs with fairly high probability. Resonances should be seen in the rate of $Na(3\,^2P_{1/2})$ production as a function of trap-laser detuning, as in the PAI spectrum, because both PAI and the process that produces $Na(3\,^2P_{1/2})$ share the same excitation pathway. The production of $Na(3\,^2P_{1/2})$ can be measured by resonant two-photon ionization, for example.

A second prediction deals with the modification of the envelope of the PAI spectrum as the temperature or trap-laser intensity is varied. Due to several competing factors, centrifugal barriers in the field dressed potentials of the entrance channels are largest for values of J that make the largest contribution to the central part of the PAI spectrum. These barriers can be raised and lowered by decreasing or increasing the laser intensity, which determines how much of the attractive 0_g^- state is radiatively mixed into the field dressed state. Preliminary calculations show that as the temperature or laser intensity is lowered the central peaks in the PAI spectrum are suppressed due to reflection of the incoming flux at the centrifugal barriers.

Finally, we would like to suggest an interesting two-color experiment involving a second laser of weak intensity that is detuned slightly (e.g., 0.3 GHz) to the blue of resonance. The idea is to turn off PAI and the fine-structure-changing process by exciting to a repulsive intermediate state with the blue detuned laser before (i.e., at larger separation) the red detuned trapping laser excites to the 0_g^- state. In Fig. 2 one sees that there are repulsive intermediate states of 0_g^+, 1_g, and 2_g symmetry that correlate at large separation to $S_{1/2}+P_{3/2}$. Based on the transition dipoles calculated from the long-range wave functions we find that the 1_g state is strongly radiatively coupled to the $\Sigma=0$ entrance channel and the 0_g^+ and 2_g states are strongly radiatively coupled to the $\Sigma=\pm 1$ entrance channels. Colliding atoms that are excited by the blue detuned laser will be reflected by these repulsive potentials back to large separation before absorption of a second photon can occur. Experimental evidence of this effect would be a decrease in the rate coefficient for Na_2^+ and $Na(3\,^2P_{1/2})$ production, and possibly an increase in fluorescence from the trap due to an increase in the density of trapped atoms, because trap loss due to PAI and fine-structure-changing transitions is suppressed. Of course the blue detuned laser must be sufficiently weak to keep it from disrupting the trapping force.

VI. CONCLUSION

In this paper we studied the PAI reaction of ultracold Na in an optical trap by using close-coupling quantum scattering theory to calculate the PAI rate coefficient as a function of the laser detuning from the $Na(^2S_{1/2}, F=2)\rightarrow Na(^2P_{3/2}, F=3)$ transition. We first calculated the long-range potentials of the intermediate and doubly excited states, and using a knowledge of these potentials and of the nature of the free-atom optical pumping process—as well as information obtained from high-temperature experiments [20–22] and theoretical studies of the autoionization step [19]—we proposed a sequential excitation mechanism involving the $^3\Sigma_u^+$ ground state, 0_g^- and 1_g intermediate states, and a 1_u doubly excited state. We found that fine-structure-changing transitions played a role in the doubly excited state, because of the 1_u avoided crossing, but not in the intermediate states as assumed by Gallagher [11], because the intermediate states involved in the trapping phase PAI have gerade symmetry and the only intermediate states that have been shown to undergo fine-structure-changing transitions with high probability have ungerade symmetry [12].

Three models differing in complexity were developed: the most accurate model used a molecule-field interaction that was molecular orientation dependent; a second model used an orientation-independent molecule-field interaction; and the simplest model used an orientation-independent interaction and was based on $\Delta J=0$ rather than $\Delta J=0,\pm 1$ selection rules. The detunings were large enough to neglect spontaneous emission, and the autoionization step was stimulated by coupling the 1_u state to an artificial channel. The PAI spectra (PAI rate coefficient versus laser detuning) calculated using the three models displayed broad peaks, which occurred at detunings two-photon resonant with the lower rotational levels ($J''<11$) of a 1_u vibrational level lying 9 GHz below the dissociation threshold, and narrow peaks, which occurred at detunings one-photon resonant with the 0_g^- vibrational levels. The ratio of computational effort associated with the three models was found to be about 50:5:1.

We also studied the effects of orientation averaging and optical pumping by calculating the PAI probability for a particular transition over a small range of detuning using the most accurate model and different level structures. We found that these effects led to a broadening to the spectrum, which we simulated by convolving the calculated spectrum with a narrow Lorentzian. When this was done the broad peaks due to two-photon resonances with the 1_u rotational levels survived and the narrow peaks due to one-photon resonances with the 0_g^- vibrational levels were either washed out or appeared as bumps or shoulders on the broad peaks. We found that the broadened spectra calculated using the three models were in good agreement with each other, which allowed us to use the simplest model to study the sensitivity of the PAI spectrum to features of the 1_u excited-state potentials and to the strength of the artificial channel coupling.

Qualitatively, the broadened spectra were in fairly good agreement with the experimental spectrum of Lett *et al.* [16]: all displayed a series of broad peaks between -0.5 and -4 GHz detuning, as well as a cutoff in the PAI signal at around -5 GHz. Quantitatively, the rate coefficient calculated using a single 1_u state was about an order of magnitude too high. Better agreement between theory and experiment, about a factor of 4 too high, was obtained when a 1_u avoided crossing, similar to the one in the 1_u potentials of Krauss [42], was added to the model.

Finally, we would like to mention several possible sources of inaccuracy which may account for why the

calculated PAI rate coefficient is too high. First, there is a need for a more quantitative understanding of long-range curve crossings ($20a_0$ or larger) in the doubly excited state that can modify the AI probability as the temperature goes to zero. Second, Dulieu, Giusti-Suzor, and Masnou-Seeuws [55] have shown that the AI probability versus energy shows complex resonance structure due to interference between "direct" and "indirect" autoionization mechanisms. Therefore we may not be justified in using the high-temperature AI probability, which was based on the high-temperature isotropic cross section, to determine our choice of the coupling strength between the doubly excited 1_u state and the artificial channel. And third, approximations associated with simplifying the full three-dimensional aspects of the collision problem might be at fault. These possible sources of error warrant further investigation.

ACKNOWLEDGMENTS

We wish to thank Dr. M. Krauss for the use of his potentials, and Dr. P. Lett, Dr. W. Phillips, and Dr. S. Rolston for permission to publish their PAI spectrum and for helpful discussions. This work is supported in part by the Office of Naval Research.

[1] See, for example, the thematic issue on laser cooling and trapping, J. Opt. Soc. Am. B **6** (1989).
[2] S. Rolston and W. D. Phillips, IEEE Proc. **79**, 943 (1991).
[3] J. Vigue, Phys. Rev. A **34**, 4476 (1986).
[4] P. Julienne, Phys. Rev. Lett. **61**, 698 (1988).
[5] P. S. Julienne and F. H. Mies, J. Opt. Soc. Am. B **6**, 2257 (1989).
[6] J. Weiner, J. Opt. Soc. Am. B **6**, 2270 (1989).
[7] A. Gallagher and D. E. Pritchard, Phys. Rev. Lett. **63**, 957 (1989).
[8] P. S. Julienne, R. Heather, and J. Vigue, in *Spectral Line Shapes,* edited by L. Frommhold and J. Keto, AIP Conf. Proc. No. 216 (American Institute of Physics, New York, 1990), Vol. 6, p. 191.
[9] P. S. Julienne, R. Heather, and J. Vigue, in *Atomic Physics,* edited by J. C. Zorn, R. R. Lewis, and M. K. Weiss (American Institute of Physics, New York, 1991), p. 116.
[10] A. M. Smith and K. Burnett, J. Opt. Soc. Am. B **8**, 1592 (1991).
[11] A. Gallagher, Phys. Rev. A **44**, 4249 (1991).
[12] P. S. Julienne and J. Vigue, Phys. Rev. A **44**, 4464 (1991).
[13] P. S. Julienne, A. M. Smith, and K. Burnett (unpublished).
[14] E. Tiesinga, B. J. Verhaar, H. T. C. Stoof, and D. van Bragt, Phys. Rev. A **45**, R2671 (1992).
[15] H. R. Thorsheim, J. Weiner, and P. S. Julienne, Phys. Rev. Lett. **58**, 2420 (1987).
[16] P. D. Lett, P. S. Jessen, W. D. Phillips, S. L. Rolston, C. I. Westbrook, and P. L. Gould, Phys. Rev. Lett. **67**, 2139 (1991).
[17] P. L. Gould, P. D. Lett, P. S. Julienne, W. D. Phillips, H. R. Thorsheim, and J. Weiner, Phys. Rev. Lett. **60**, 788 (1988).
[18] P. S. Julienne and R. Heather, Phys. Rev. Lett. **67**, 2135 (1991).
[19] A. Henriet, O. Dulieu, and F. Masnou-Seeuws, Z. Phys. D **18**, 287 (1991); O. Dulieu, A. Giusti-Suzor, and F. Masnou-Seeuws, J. Phys. B **24**, 4391 (1991).
[20] N. N. Bezuglov, A. N. Klucharev, and V. A. Sheverev, J. Phys. B **20**, 2497 (1987).
[21] J. Weiner, F. Masnou-Seeuws, and A. Giusti-Suzor, Adv. At. Mol. Opt. Phys. **26**, 209 (1989), and references therein.
[22] H. A. J. Meijer, Z. Phys. D **17**, 257 (1990), and references therein.
[23] Y. B. Band and P. S. Julienne, Phys. Rev. A **46**, 330 (1992).
[24] J. Dalibard and C. Cohen-Tannoudji, J. Opt. Soc. Am. B **2**, 1707 (1985).
[25] See, for example, G. Herzberg, *Spectra of Diatomic Molecules* (Van Nostrand Reinhold, New York, 1950), p. 219.
[26] D. D. Konowalow, M. E. Rosenkrantz, and M. L. Olson, J. Chem. Phys. **72**, 2612 (1980).
[27] G. Jeung, J. Phys. B **16**, 4289 (1983).
[28] M. Y. Ovchinnikova, Theor. Expt. Chem. **1**, 22 (1965); E. I. Dashevskaya, A. I. Voronin, and E. E. Nikitin, Can. J. Phys. **47**, 1237 (1969).
[29] M. E. Kaminsky, J. Chem. Phys. **66**, 4951 (1977).
[30] P. Kusch and M. M. Hessel, J. Chem. Phys. **68**, 2591 (1978).
[31] B. Linder and J. O. Hirschfelder, J. Chem. Phys. **28**, 197 (1958).
[32] Based on the effective charge seen by the Na ($3P$) electron.
[33] S. Geltman, J. Phys. B **21**, L735 (1988); **22**, 2049 (1989).
[34] A. Henriet and F. Masnou-Seeuws, J. Phys. B **23**, 219 (1990).
[35] W. C. Stwalley, Y.-H. Yang, and G. Pichler, Phys. Rev. Lett. **41**, 1164 (1978).
[36] B. Bussery and M. Aubert-Frecon, J. Chem. Phys. **82**, 3224 (1985).
[37] B. Bussery and M. Aubert-Frecon, J. Mol. Spectrosc. **113**, 21 (1985).
[38] P. Kowalcyzk, Chem. Phys. Lett. **68**, 203 (1979).
[39] J. T. Hougen, Nat. Bur. Stand. (U.S.) Monogr. **115**, 1 (1979).
[40] H. Lefebvre-Brion and R. W. Field, *Perturbations in the Spectra of Diatomic Molecules* (Academic, Orlando, 1986), p. 115.
[41] W. H. Louisell, *Quantum Statistical Properties of Radiation* (Wiley, New York, 1973), p. 273.
[42] M. Krauss (private communication).
[43] M. Krauss and W. Stevens, J. Chem. Phys. **93**, 4236 (1990).
[44] R. J. LeRoy and R. B. Bernstein, J. Chem. Phys. **52**, 3869 (1970).
[45] L. D. Landau, Phys. Z. Sow. **1**, 46 (1932); C. Zener, Proc. R. Soc. London Ser. A **137**, 696 (1932).
[46] H. Nakamura, J. Phys. Soc. Jpn. **31**, 574 (1971).
[47] R. J. Bieniek, Phys. Rev. A **18**, 392 (1978).
[48] K. S. Lam and T. F. George, Phys. Rev. A **32**, 1650 (1985).
[49] X. Urbain, A. Giusti-Suzor, D. Fussen, and C. Kubach, J. Phys. B **19**, L273 (1986).
[50] R. A. Gordon, J. Chem. Phys. **51**, 14 (1969).
[51] J. M. Launay, J. Phys. B **10**, 3665 (1977).
[52] P. S. Julienne and F. H. Mies, Phys. Rev. A **25**, 3399 (1982).
[53] J. C. Peploski and L. Eno, J. Chem. Phys. **89**, 3579 (1988).
[54] P. L. DeVries and T. F. George, Phys. Rev. A **18**, 1751 (1978).
[55] O. Dulieu, A. Giusti-Suzor, and A. Masnou-Seeuws, J. Phys. B (to be published).